

1 **Boundary of nighttime ozone chemical equilibrium in the mesopause region: long-**
2 **term evolution determined using 20-year satellite observations**

3 Mikhail Yu. Kulikov¹, Mikhail V. Belikovich¹, Aleksey G. Chubarov¹, Svetlana O. Dementyeva¹, and
4 Alexander M. Feigin¹

5 ¹A. V. Gaponov-Grekhov Institute of Applied Physics of the Russian Academy of Sciences, 46 Ulyanov
6 Str., 603950 Nizhny Novgorod, Russia

7 Correspondence to: Mikhail Yu. Kulikov (mikhail_kulikov@mail.ru)

8

9 **Abstract.** The assumption of nighttime ozone chemical equilibrium (NOCE) is widely employed for
10 retrieving the O_x - HO_x components in the mesopause from rocket and satellite measurements. In this
11 work, the recently developed analytical criterion of determining the NOCE boundary is used (i) to study
12 the connection of this boundary with O and H spatiotemporal variability based on 3D modeling of
13 chemical transport, and (ii) to retrieve and analyze the spatiotemporal evolution of the NOCE boundary in
14 2002-2021 from the SABER/TIMED data set. It was revealed, first, that the NOCE boundary reproduces
15 well the transition zone dividing deep and weak photochemical oscillations of O and H caused by the
16 diurnal variations of solar radiation. Second, the NOCE boundary is sensitive to sporadic abrupt changes
17 in the middle atmosphere dynamics, in particular, due to powerful sudden stratospheric warmings leading
18 to the events of an elevated (up to ~80 km) stratopause, which took place in January-March 2004, 2006,
19 2009, 2010, 2012, 2013, 2018, and 2019. Third, the space-time evolution of this characteristic expressed
20 via pressure altitude contains a clear signal of 11-year solar cycle in the 55°S-55°N range. In particular,
21 the mean annual NOCE boundary averaged in this range of latitudes anticorrelates well with $F_{10.7}$ index
22 with the coefficient -0.95. Moreover, it shows a weak linear trend of the 56.2 ± 42.2 m/decade.

23

24 **1 Introduction**

25 The mesopause (80-100 km) is an interesting region of the Earth's atmosphere possessing quite a
26 number of unique phenomena and processes which can be considered as sensitive indicators/predictors of
27 global climate change and anthropogenic influences on atmospheric composition (e.g., Thomas et al.,
28 1989). Here, the summer temperature at middle and high latitudes reaches its lowest values (down to
29 100K (Schmidlin, 1992)). The temperatures below 150K lead to water vapour condensation and
30 formation of the highest altitude clouds in the Earth's atmosphere, the so-called Polar Mesospheric
31 Clouds or Noctilucent Clouds consisting primarily of water ice (Thomas, 1991). In turn, the temperature
32 of the winter mesopause is essentially higher, so there is a strong negative temperature gradient between
33 the summer and winter hemispheres. At these altitudes, atmospheric waves of various spatiotemporal
34 scales are observed, in particular, internal gravity waves coming from the lower atmosphere. Destruction
35 of gravity waves leads to strong turbulence that affects the atmospheric circulation and ultimately
36 manifests itself in the mentioned temperature structure of this region.

37 Many layer phenomena in the mesopause are related to the photochemistry of the O_x - HO_x
38 components (O, O_3 , H, OH, and HO_2). There is a narrow (in height) transition region where
39 photochemistry behaviour transforms rapidly from "deep" diurnal oscillations, when the difference
40 between daytime and nighttime values of the O_x - HO_x components can reach several orders of magnitude,
41 to weak photochemical oscillations. As a result, above this region, O and H accumulate to form the

42 corresponding layers. This layer formation manifests itself in the appearance of a secondary ozone
43 maximum and airglow layers of OH and O excited states. Thus, O_x-HO_x photochemistry in the
44 mesopause is responsible for the presence of important (first of all, from a practical point of view)
45 indicators observed in the visible and infrared ranges, which are widely used for ground-based and
46 satellite monitoring of climate changes and wave activity. Moreover, O_x-HO_x photochemistry provides
47 the total chemical heating rate of this region, influences the radiative cooling and other useful airglows
48 (for example, by O₂ excited states), is involved in the plasma-chemical reactions and formation of layers
49 of the ionosphere. The mentioned transformation of O_x-HO_x behaviour with height may occur via the
50 nonlinear response of O_x-HO_x photochemistry to the diurnal variations of solar radiation in the form of
51 subharmonic (with periods of 2, 3, 4, and more days) or chaotic oscillations (e.g., Sonnemann and
52 Fichtelmann, 1997; Feigin et al., 1998). This unique phenomenon was predicted many years ago
53 (Sonnemann and Fichtelmann, 1987) and investigated theoretically by models taking into account
54 different transport processes (Sonnemann and Feigin, 1999; Sonnemann et al., 1999; Sonnemann and
55 Grygalashvyly, 2005; Kulikov and Feigin, 2005; Kulikov, 2007; Kulikov et al., 2020). It was revealed, in
56 particular, that the nonlinear response is controlled by vertical eddy diffusion (Sonnemann and Feigin,
57 1999; Sonnemann et al., 1999), so that 2-day oscillations can only survive at real diffusion coefficients,
58 but the eddy diffusion in zonal direction leads to the appearance of the so-called reaction-diffusion waves
59 in the form of propagating phase fronts of 2-day oscillations (Kulikov and Feigin, 2005; Kulikov et al.,
60 2020). Recently, the satellite data processing revealed the first evidence of the existence of 2-day
61 photochemical oscillations in the real mesopause (Kulikov et al., 2021).

62 While regular remote sensing measurements of most O_x-HO_x components are still limited, the
63 indirect methods based on the physicochemical assumptions are useful tools for monitoring these trace
64 gases. In many papers, O and H distributions were retrieved from the daytime and nighttime rocket and
65 satellite measurements of the ozone and the volume emission rates of OH(v), O(¹S), and O₂(a¹Δ_g) (Good,
66 1976; Pendleton et al., 1983; McDade et al., 1985; McDade and Llewellyn, 1988; Evans et al., 1988;
67 Thomas, 1990; Llewellyn et al., 1993; Llewellyn and McDade, 1996; Mlynczak et al., 2007, 2013a,
68 2013b, 2014, 2018; Smith et al., 2010; Xu et al., 2012; Siskind et al., 2008, 2015). The retrieval technique
69 is based on the assumption of ozone photochemical/chemical equilibrium and physicochemical model of
70 the corresponding airglow, which describe the relationship between local O and H values and
71 measurement data.

72 The daytime photochemical ozone equilibrium is a good approximation everywhere in the
73 mesosphere – lower thermosphere (MLT) region (Kulikov et al., 2017) due to ozone photodissociation,
74 whereas the applicability of the assumption of nighttime ozone chemical equilibrium (NOCE) is limited:
75 there is an altitude boundary above which NOCE is satisfied to an accuracy better than 10%. Below this

76 boundary, the ozone equilibrium is disturbed essentially and cannot be used. Good (1976) supposed that
77 NOCE is fulfilled above 60 km, whereas other papers apply the NOCE starting from 80 km, independent
78 of latitude and season. However, studies of NOCE within the framework of the 3D chemical-transport
79 models (Belikovich et al., 2018; Kulikov et al., 2018a) revealed that the NOCE boundary varies within
80 the range of 81–87 km, depending on latitude and season. In view of the practical need to determine the
81 local altitude position of this boundary, Kulikov et al. (2018a) presented a simple criterion determining
82 the equilibrium boundary using only the data provided by the SABER (Sounding of the Atmosphere
83 using Broadband Emission Radiometry) instrument onboard the TIMED (Thermosphere Ionosphere
84 Mesosphere Energetics and Dynamics). Making use of this criterion, Kulikov et al. (2019) retrieved the
85 annual evolution of the NOCE boundary from the SABER data. It was revealed that a two-month
86 averaged NOCE boundary essentially depends on season and latitude and can rise up to ~ 86 km.
87 Moreover, the analysis of the NOCE boundary in 2003-2005 showed that this characteristic was sensitive
88 to unusual dynamics of stratospheric polar vortex during the 2004 Arctic winter, which was named a
89 remarkable winter in the 50-year record of meteorological analyses (Manney et al., 2005). Moreover,
90 Belikovich et al. (2018) found by 3D simulation that the excited OH layer repeats well spatiotemporal
91 variability of the NOCE boundary. These results allowed us to speculate that the NOCE boundary can be
92 considered as an important indicator of mesopause processes.

93 The main goals of this paper are (1) to investigate the relationship between the NOCE boundary
94 according to the mentioned criterion and O and H variability with the use of the 3D chemical transport
95 model, and (2) to retrieve and analyze the spatiotemporal evolution of the NOCE boundary in 2002-2021
96 from the SABER/TIMED data set. In the next section, we present the used model. In Section 3, we briefly
97 describe the criterion of determining the NOCE boundary local height and study how this height is related
98 to the features of O and H distributions from the 3D model. Section 4 explains the methodology of
99 determining the NOCE boundary from satellite data. Section 5 presents the main results obtained from
100 SABER/TIMED data discussed in Section 6.

101

102 **2 3D model**

103 We use the 3D chemical transport model of the middle atmosphere developed by the Leibniz
104 Institute of Atmospheric Physics (Sonnemann et al., 1998; Körner and Sonnemann, 2001; Grygalashvyly
105 et al., 2009; Hartogh et al., 2004, 2011). The three-dimensional fields of temperature and winds were
106 adopted by Kulikov et al. (2018b) from the Canadian Middle Atmosphere Model (Scinocca et al., 2008)
107 for the year 2000 with an updated frequency of 6 hours. To exclude unrealistic jumps in the evolution of
108 calculated chemical characteristics, linear smoothing between two subsequent updates of these parameters

109 is applied. The model takes into account 3D advective transport and vertical diffusive transport (both,
 110 turbulent and molecular). The Walcek-scheme (Walcek, 2000) and the implicit Thomas algorithm
 111 (Morton and Mayers, 1994) are used for advective and diffusive transport, respectively. The model grid
 112 includes 118 pressure-height levels (from the ground to ~135 km), 32 and 64 levels in latitude and
 113 longitude, respectively. The chemical part considers 22 constituents (O, O(¹D), O₃, H, OH, HO₂, H₂O₂,
 114 H₂O, N, NO, NO₂, NO₃, N₂O, CH₄, CH₂, CH₃, CH₃O₂, CH₃O, CH₂O, CHO, CO, CO₂), 54 two- and
 115 three-body reactions, and 15 photo-dissociation reactions. The model uses pre-calculated dependences of
 116 dissociation rates on altitude and solar zenith angle (Kremp et al., 1999). The chemistry is calculated by
 117 the Shimazaki scheme (Shimazaki, 1985) for the integration time of 9 sec.

118

119 3 The NOCE criterion

120 The nighttime ozone chemistry at the mesopause heights is determined mainly by two reactions R1-
 121 R2 (e.g., Allen et al., 1984), see Table 1. The secondary ozone loss via the O + O₃ → 2O₂ reaction
 122 becomes important above ~ 95 km (Smith et al., 2009). Kulikov et al. (2023) verified with simulated and
 123 measured data that this reaction does not influence the NOCE boundary determination and may be
 124 skipped. Thus, the ozone equilibrium concentration (O_3^{eq}) corresponding to the instantaneous balance
 125 between the production and loss terms is as follows:

$$126 \quad O_3^{eq} = \frac{k_1 \cdot O \cdot O_2 \cdot M}{k_2 \cdot H}, \quad (1)$$

127 where M is air concentration, and k_{1-2} are the corresponding rate constants of the reactions (see Table 1).

128 As mentioned above, the NOCE criterion was developed in Kulikov et al. (2018a). The main idea is
 129 that the local values of O_3 and O_3^{eq} are close ($O_3(t) \approx O_3^{eq}(t)$), when $\tau_{O_3} \ll \tau_{O_3^{eq}}$, where τ_{O_3} is the
 130 ozone lifetime and $\tau_{O_3^{eq}}$ is the local time scale of O_3^{eq} :

$$131 \quad \tau_{O_3} = \frac{1}{k_2 \cdot H}, \quad (2)$$

$$132 \quad \tau_{O_3^{eq}} \equiv \frac{O_3^{eq}}{|dO_3^{eq}/dt|} = \frac{O}{H \cdot \left| \frac{d}{dt} \left(\frac{O}{H} \right) \right|}. \quad (3)$$

133 As shown in Kulikov et al. (2018a), $\tau_{O_3^{eq}}$ can be determined from a simplified photochemical model
 134 describing the O_x-HO_x evolution in the mesopause region (Feigin et al., 1998), so the criterion of the
 135 NOCE validity can be written in the form:

$$136 \quad Cr = \frac{\tau_{O_3}}{\tau_{O_3^{eq}}} = 2 \frac{k_1 \cdot k_4 \cdot O_2^2 \cdot M^2}{k_2} \left(1 - \frac{k_5 + k_6}{k_3} \right) \cdot \frac{1}{k_2 \cdot H \cdot O_3} \ll 1, \quad (4)$$

137 where k_i are the corresponding reaction constants from Table 1. Calculations with the global 3D
 138 chemistry-transport model of the middle atmosphere showed (Kulikov et al. 2018a) that the criterion
 139 $\tau_{O_3}/\tau_{O_3^{eq}} \leq 0.1$ defines well the boundary of the area where $|O_3/O_3^{eq} - 1| \leq 0.1$.

140 Kulikov et al. (2023) presented the theory of chemical equilibrium of a certain trace gas n . Strictly
 141 mathematically, the cascade of sufficient conditions for $n_i(t) \cong n_i^{eq}(t)$ was derived considering its
 142 lifetime, equilibrium concentration, and time dependences of these characteristics. In case of the
 143 nighttime ozone, it was proved that $\tau_{O_3}/\tau_{O_3^{eq}} \ll 1$ is the main condition for NOCE validity and the
 144 criterion $\tau_{O_3}/\tau_{O_3^{eq}} \leq 0.1$ limits a possible difference between O_3 and O_3^{eq} to not more than $\sim 10\%$.
 145 Moreover, Kulikov et al. (2023) slightly corrected the expression for the criterion (4):

$$146 \text{ Cr} = 2 \frac{k_1 \cdot O_2 \cdot M}{k_2} (k_4 \cdot M \cdot O_2 \cdot \left(1 - \frac{k_5 + k_6}{k_3}\right) + k_2 \cdot O_3) \cdot \frac{1}{k_2 \cdot H \cdot O_3} \leq 0.1. \quad (5)$$

147 One more important condition for $O_3 \approx O_3^{eq}$ at the time moment t is:

$$148 e^{\int_{t_{bn}}^t \tau_{O_3}^{-1} dt} \gg 1, \quad (6)$$

149 where t_{bn} is the time of the beginning of the night. The ozone equilibrium concentration jumps at sunset
 150 due to the shutdown of photodissociation. Thus, the condition (6) shows that it takes time for the ozone
 151 concentration to reach a new equilibrium. Kulikov et al. (2023) revealed that, at the solar zenith angle $\chi >$
 152 95° , the condition (6) is fulfilled almost in all cases and the condition (5) becomes the main criterion for
 153 NOCE validity. In addition, Kulikov et al. (2023) demonstrated with the use of a 3-D model that the
 154 criterion (5) almost ideally reproduces the NOCE boundary found by direct comparison of O_3 and O_3^{eq}
 155 concentrations, see Figure 1 in Kulikov et al. (2023).

156 Figures 1-3 demonstrate model examples of O and H time-height variations above different points
 157 over three months. In order to focus attention on diurnal oscillations, the concentrations are normalized by
 158 mean daily values, which were calculated as a function of altitude. These daily average O and H values
 159 were different for each altitude. One can see in all panels of these figures "deep" diurnal oscillations that
 160 occur below 81-87 km. Due to the shutdown of sources at night and high rates of the main HO_x and O
 161 sinks nonlinearly dependent on air concentration (Konovalov and Feigin, 2000), the variables change
 162 during each night within the range of several orders of magnitude with low values of time evolution.
 163 Above 83-88 km, the situation differs essentially from the previous case. One can see relatively weak
 164 diurnal oscillations. These regimes of O and H behaviour are consistent, i.e. deep H diurnal oscillations
 165 correspond to the same dynamics in O, and so on. There exists a few-km thick layer (transition zone)
 166 dividing deep and weak oscillations whose height position depends on latitude and season. In particular,
 167 in summer the middle latitude transition is higher than in winter. Figures 1-3 show also the magenta lines
 168 pointing the NOCE boundary in accordance with the criterion (5) ($\text{Cr} = 0.1$). One can see that the NOCE

169 criterion almost perfectly reproduces the features of the transition zone. Thus, our criterion is not only a
 170 useful technical characteristic to retrieve O from satellite data, but it also points to an important
 171 dynamical process in the O_x-HO_x photochemistry.

172

173 **4 NOCE boundary from satellite data**

174 We use version 2.0 of the SABER data product (Level2A) for the simultaneously measured profiles
 175 of pressure (p), altitude (z), temperature (T), O₃ (at 9.6 μm), and total volume emission rates of OH*
 176 transitions at 2.0 (VER) within the 0.0001–0.02 mbar pressure interval (altitudes approximately 75–105
 177 km) in 2002–2021. We consider only nighttime data when the solar zenith angle $\chi > 95^\circ$.

178 Kulikov et al. (2018a) noted that the term $k_2 \cdot H \cdot O_3$ in the expression for the NOCE criterion can
 179 be rewritten in the form depending on measurable characteristics only with the use of the corresponding
 180 OH(ν) model by Mlynczak et al. (2013a):

$$181 \quad k_2 \cdot H \cdot O_3 = VER/A(T, M, O), \quad (7)$$

182 where $A(T, M, O)$ is the function in square brackets in Eq. (3) in the paper by Mlynczak et al. (2013a)
 183 with the parameters corrected by Mlynczak et al. (2018):

$$184 \quad A(T, M, O) =$$

$$185 \quad \frac{0.47 \cdot 118.35}{215.05 + 2.5 \cdot 10^{-11} \cdot O_2 + 3.36 \cdot 10^{-13} \cdot e^{\frac{220}{T}} \cdot N_2 + 3 \cdot 10^{-10} \cdot O} + \frac{0.34 \cdot 117.21}{178.06 + 4.8 \cdot 10^{-13} \cdot O_2 + 7 \cdot 10^{-13} \cdot N_2 + 1.5 \cdot 10^{-10} \cdot O} +$$

$$186 \quad \frac{0.47 \cdot 117.21 \cdot (20.05 + 4.2 \cdot 10^{-12} \cdot O_2 + 4 \cdot 10^{-13} \cdot N_2)}{(215.05 + 2.5 \cdot 10^{-11} \cdot O_2 + 3.36 \cdot 10^{-13} \cdot e^{\frac{220}{T}} \cdot N_2 + 3 \cdot 10^{-10} \cdot O) \cdot (178.06 + 4.8 \cdot 10^{-13} \cdot O_2 + 7 \cdot 10^{-13} \cdot N_2 + 1.5 \cdot 10^{-10} \cdot O)}. \quad (8)$$

187 This function is the result of the combination of the equations of physicochemical OH* balance in the $\nu =$
 188 8 and $\nu = 9$ states. It depends on the constants of the processes describing sources and sinks at the
 189 corresponding levels, in particular, the OH(ν) removal on collisions with O₂, N₂, and O. Below 86–87 km,
 190 $A(T, M, O) \cong A(T, M, O = 0) \equiv A(T, M)$ due to relatively small O concentrations. Thus, by combining
 191 Eqs. (5) and (7), the NOCE criterion for SABER data can be recast in the following form:

$$192 \quad VER \geq VER_{min}(T, M) = 20 \cdot \frac{k_1 \cdot O_2 \cdot M}{k_2} (k_4 \cdot O_2 \cdot M \cdot \left(1 - \frac{k_5 + k_6}{k_3}\right) + k_2 \cdot O_3) \cdot A(T, M). \quad (9)$$

193 Due to the strong air-concentration dependence VER_{min} decreases rapidly with height. In particular,
 194 at 105 km, $VER \gg VER_{min}$. At 75 km, the relationship is inverse. We determine the local position of the
 195 NOCE boundary (pressure level p_{eq}^l and altitude level z_{eq}^l) according to the criterion (9), where
 196 $VER = VER_{min}(T, M)$. We verified that the approximation $A(T, M, O) \cong A(T, M)$ is valid near the
 197 NOCE boundary. With the use of annual SABER data, we calculated simultaneous datasets of $A(T, M)$

198 and $A(T, M, O)$. In the second case, we used O retrieved from the same SABER data. The maximum and
 199 mean differences between $A(T, M)$ and $A(T, M, O)$ were found to be $\sim 2\%$ and $\sim 0.1\%$, respectively.

200 The total range of latitudes according to the satellite trajectory over a month was $\sim(83.5^\circ\text{S} - 83.5^\circ\text{N})$.
 201 This range was divided into 20 bins and all local values of p_{eq}^l and z_{eq}^l falling into one bin during a
 202 month or a year were averaged, respectively. In particular, several thousand values of p_{eq}^l and z_{eq}^l fall
 203 into one bin during a month. Following Mlynczak et al. (2013a), averages were determined by binning
 204 the data of a certain day by local hour and then averaging over the hour bins that contain data to obtain
 205 the daily average value. Then we calculated monthly mean values of p_{eq}^m and z_{eq}^m and annually mean
 206 values of p_{eq}^y and z_{eq}^y (hereafter, the indexes «m» and «y» indicate the monthly and annually average,
 207 respectively). Then, for convenience, the values of p_{eq}^m and p_{eq}^y were recalculated into the pressure
 208 altitudes h_{eq}^m and h_{eq}^y . The dependence of $h_{eq}^{m,y}$ on $p_{eq}^{m,y}$ was adopted from Mlynczak et al. (2013a,
 209 2014):

$$210 \quad h_{eq}^{m,y} = -H_a \cdot \log(p_{eq}^{m,y}/p_0), \quad H_a = 5.753474, \quad p_0 = 11430.49428 \text{ hPa.} \quad (10)$$

211 Note that the use of both, geometrical and pressure coordinates is a rather common approach when
 212 analyzing long-term evolution of the obtained data, especially, when the data is the result of averaging
 213 over time and space. In particular, Lübken et al. (2013) demonstrated the importance of distinguishing
 214 between trends on pressure and geometrical altitudes in the mesosphere, since the second includes the
 215 atmospheric shrinking effect and is more pronounced. Grygalashvyly et al. (2014) analyzed the linear
 216 trends in OH* peak height and revealed a remarkable decrease at geometrical altitudes, which is almost
 217 absent at pressure altitudes.

218 Kulikov et al. (2023) studied the systematic uncertainty of the retrieved NOCE boundary height.
 219 Following the typical analysis presented, for example, in Mlynczak et al. (2013a, 2014), the uncertainty
 220 was obtained by calculating the root-sum-square of the individual sensitivity of the retrieved
 221 characteristic to the perturbation of O_3 , T , rates of reactions, and parameters of the A function. The
 222 systematic error of NOCE pressure altitude h_{eq}^m and geometrical altitude z_{eq}^m varied in the range of
 223 0.1-0.3 km, whereas the random error was negligible due to averaging over time and space.

224

225 **5 NOCE boundary in 2002-2021 from SABER/TIMED data: main results**

226 Figure 4 demonstrates the time evolution of the pressure altitude h_{eq}^m in 2002-2021 in all latitude
 227 bins. Figures 5 (left column) show the mean (for 2002-2021) annual cycle of h_{eq}^m at four specific
 228 latitudes and Figures 6 (left column) present the Fourier spectra at these latitudes obtained from the data

229 in Figure 4. Note, first, that above $\sim 58^\circ\text{S,N}$, there are data gaps specified by the satellite sensing
 230 geometry. For example, in 2002-2014, at $66.8\text{-}75.15^\circ\text{S,N}$ measurements covered 6 months per year only.
 231 In 2015, because of slight changes in the satellite geometry, there appeared additional months. This is
 232 especially noticeable above $\sim 66^\circ\text{S,N}$ and manifests itself by extension of the variation range of h_{eq}^m at
 233 these latitudes in 2015-2021. Second, the variation range of h_{eq}^m , annual cycle and spectrum of harmonic
 234 oscillations depends essentially on the latitude. Near the equator, h_{eq}^m varies in the 81-83 km range
 235 mainly and there are two main harmonics with periods of 1/2 and 1 year in the spectrum. At low latitudes,
 236 the variation range of h_{eq}^m narrows down to a minimum ($\sim 82\text{-}83$ km at $16.7\text{-}20.05^\circ\text{S,N}$), which is
 237 accompanied with the appearance of a wide spectrum of harmonics with periods of 1/5, 1/4, 1/3, 1/2, and
 238 1 year. At middle latitudes, the range of h_{eq}^m variation monotonically increases up to $\sim 81.5\text{-}85.5$ km with
 239 latitude and the harmonic with a period of 1 year becomes the main mode in the spectrum of oscillations.
 240 At both, low and middle latitudes, there is no signal from quasi-biennial oscillations but one can see a
 241 remarkable amplitude of a harmonic with a period of ~ 10 years, which can be associated with a
 242 manifestation of 11-year solar cycle. It is interesting that the mentioned features are typical for both
 243 hemispheres. At high latitudes, h_{eq}^m varies in the range of 79-86.5 km. At these latitudes, one can see the
 244 main difference between the northern and southern hemispheres: the sharp falls and rises of the northern
 245 boundary of NOCE by several km (up to 3-4 km) appearing in January-March 2004, 2006, 2009, 2010,
 246 2012, 2013, 2018 and 2019 that are absent at southern latitudes.

247 The analysis of Figures 5-6 demonstrates the following redistribution in the annual cycle with
 248 increasing latitude from equator to polar latitudes. Near the equator, the annual cycle has two maxima in
 249 June – July and in December – January. The first one is more pronounced. That is why there are two main
 250 harmonics with periods of 1/2 and 1 year in the spectrum. At low latitudes, one maximum (summer) does
 251 not change, while the other approaches the first one. As a result, the spectrum of harmonics is wide. At
 252 middle latitudes, the maxima gradually merge so that the 1 year-harmonic becomes the main one.

253 Figure 7 (left) demonstrates a contour map of the space-time evolution of the average annual
 254 pressure altitude h_{eq}^y in 2002-2021. Figure 8 presents the time evolution of this characteristic at different
 255 latitudes. Based on the Fourier spectra presented in Figures 6 (left column), we can suppose that, at low
 256 and middle latitudes, the interannual variation of h_{eq}^y is caused by the 11-year solar cycle mainly. Figure
 257 9 (left) presents the correlation coefficient of h_{eq}^y with $F_{10.7}$ index (solar radio flux at 10.7 cm, see the red
 258 curve in Figure 10) as a function of latitude. One can see good anticorrelation (with a coefficient from -
 259 0.72 to -0.92) between $\sim 55^\circ\text{S}$ and $\sim 55^\circ\text{N}$. At high latitudes, the absolute value of the correlation
 260 coefficient decreases sharply down to ~ 0.58 in the south and to ~ 0.1 in the north. The blue curve in Figure

261 10 shows latitude-averaged h_{eq}^y in the range of 55°S-55°N. In this case, the anticorrelation with $F_{10.7}$
262 index is close to ideal (coefficient ~ -0.95).

263 With the use of multiple linear regression in the 55°S-55°N range:

$$264 \quad h_{eq}^y(\text{year}) = \text{const} + \alpha \cdot \text{year} + \beta \cdot F_{10.7}(\text{year}), \quad (11)$$

265 we determined a slow (up to 10 m/year) linear trend of h_{eq}^y as a function of latitude, but with the
266 uncertainties essentially larger than the trend values. Applying the regression analysis to latitude-averaged
267 h_{eq}^y (blue curve in Figure 10) gave us a more statistically significant value of the trend: 5.62 ± 4.22
268 m/year.

269 Figure 11 demonstrates the time evolution of the geometrical altitude z_{eq}^m in 2002-2021 in all
270 latitude bins. Figures 5 (right column) show the mean (for 2002-2021) annual cycle of z_{eq}^m at four
271 specific latitudes and Figures 6 (right column) present the Fourier spectra at these latitudes obtained from
272 the data in Figure 11. Comparison with Figures 4 and 5-6 (left columns) shows that z_{eq}^m repeats many
273 qualitative features of the space-time evolution of pressure altitude h_{eq}^m . In particular, in the direction
274 from the equator to the poles, the variation range of z_{eq}^m first decreases down to 1 km at 16°-25°S,N and
275 then expands to several km at middle and high latitudes. One can see the same redistribution of the annual
276 cycle with latitude, similarly to the pressure altitude case. Near the equator, the annual cycle possesses
277 two maxima occurring in June – July and in December – January. At low latitudes, one maximum
278 continues in summer, whereas the other shifts to spring. At middle latitudes, the maxima gradually
279 coalesce forming a single summer maximum. At high northern latitudes, there are the same local sharp
280 variations of the NOCE boundary in January-February 2004, 2006, 2009, 2010, 2012, 2013, 2018 and
281 2019, which are absent at southern latitudes. One can see from Figure 5 that, on the average, z_{eq}^m is
282 lower than h_{eq}^m by 0.5-1 km, depending on latitude. One can see from Figure 6 that the z_{eq}^m spectra of
283 harmonic oscillations are similar to the h_{eq}^m spectra except for the absence of a signal of the 11-year
284 solar cycle.

285 Figure 7(right) demonstrates a contour map of space-time evolution of the annually average
286 geometrical altitude z_{eq}^y in 2002-2021. Figure 12 presents the time evolution of this characteristic at
287 different latitudes. One can see that there is no clear evidence of 11-year solar cycle manifestation at all
288 latitudes. This is confirmed by the calculation of the correlation coefficient of z_{eq}^y with $F_{10.7}$ index as a
289 function of latitude (see Figure 9 (right)). Moreover, the latitude-averaged (in the range of 55°S-55°N)
290 z_{eq}^y has a correlation coefficient equal to ~ -0.55 .

291 As in the case of h_{eq}^y , we found with the use of multiple linear regression the slow (up to \sim -10
292 m/year) and statistically insignificant linear trend of z_{eq}^y as a function of latitude. Moreover, the
293 regression analysis of latitude-averaged z_{eq}^y also revealed a statistically insignificant trend.

295 **6 Discussion**

296 The NOCE boundary is an important technical characteristic for correct application of the NOCE
297 approximation to retrieve the nighttime distributions of minor chemical species of MLT. Kulikov et al.
298 (2019) repeated the O and H retrieval by Mlynczak et al. (2018) from the SABER data for the year 2004.
299 It was revealed that the application of the NOCE condition below the boundary obtained according to the
300 criterion could lead to a great (up to 5–8 times) systematic underestimation of O concentration below 86
301 km, whereas it was insignificant for H retrieval. The results presented in Figures 4, 5 and 11 demonstrate
302 that, except for high northern latitudes, there is a stable annual cycle of the NOCE boundary. The monthly
303 mean boundary can rise up to geometrical altitudes of 82-83 km ($\sim(5.2-6.2) \cdot 10^{-3}$ hPa) at low latitudes and
304 up to 84-85 km ($\sim(3.7-4.4) \cdot 10^{-3}$ hPa) at middle and high latitudes. Thus, the SABER O data below these
305 altitudes/pressures may be essentially incorrect and the retrieval approaches without using the NOCE
306 condition (e.g., Panka et al., 2018) should be more appropriate.

307 Note that the NOCE condition was used not only for O and H derivation from satellite data. This
308 assumption is a useful approach helping (i) to study hydroxyl emission in the MLT region with simulated
309 and measured data, in particular, OH* mechanisms, morphology and variability caused, for example, by
310 atmospheric tides and gravity wave activity (e.g., Marsh et al., 2006; Nikoukar et al., 2007; Xu et al.,
311 2010, 2012; Kowalewski et al., 2014; Sonnemann et al., 2015); (ii) to analyze the MLT response to
312 sudden stratospheric warmings (SSWs) (e.g., Smith et al., 2009); (iii) to derive exothermic heating rates
313 of MLT (e.g., Mlynczak et al., 2013b); (iv) to analytically simulate the mesospheric OH* layer response
314 to gravity waves (e.g., Swenson and Gardner, 1998); and (v) to derive the analytical dependence of
315 excited hydroxyl layer number density and peak altitude on atomic oxygen and temperature (e.g.,
316 Grygalashvyly et al., 2014; Grygalashvyly, 2015). Perhaps some results require revision or reanalysis
317 taking the NOCE boundary into account. For example, Smith et al. (2009) used the NOCE condition to
318 analyze the ozone perturbation in the MLT, in particular, during the SSW at the beginning of 2009 (the
319 central day was January 24). Our preliminary results of processing the SABER and simulated data in
320 January 2009 show that the NOCE boundary above 70°N may jump from \sim 80 km to \sim 90-95 km due to a
321 short-time abrupt temperature fall above 80 km during this SSW. Thus, one can assume that the NOCE
322 condition is not a good approximation for the description of ozone variations directly in the process of

323 SSWs. This case will be studied in a separate work. Note also that after the SSW of January 2009 there
 324 began a long-time (several tens of days) event of elevated (up to ~80-85 km) stratopause (see, e.g., Figure
 325 1 in Smith et al. (2009)), which led to the corresponding increase of temperature above 80 km. The
 326 occurrence of this event and its duration are in a good correlation with sharp lowering of the NOCE
 327 boundary at high northern latitudes (see Figures 4 and 11). Moreover, all abrupt changes of the NOCE
 328 boundary at these latitudes in January-March of other years (2004, 2006, 2010, 2012, 2013, 2018, and
 329 2019) can be also associated with the elevated stratopause events in these years (see García-Comas et al.
 330 (2020) and references there).

331 According to the used chemical-transport model, the NOCE boundary reproduces well the transition
 332 zone dividing deep and weak diurnal oscillations of O and H (see Figures 1-3). We verified this feature
 333 with the annual run of SD-WACCM-X model for the year 2017 provided by the NCAR High Altitude
 334 Observatory (<https://doi.org/10.26024/5b58-nc53>). Despite the low time resolution of the downloaded
 335 data (3-hour averaging), we obtained the results (see Figure 13) similar to Figures 1-3. Note also that both
 336 models give the same consistence between the altitudes of the NOCE boundary and the mentioned
 337 transition zone at high latitudes in spring and autumn.

338 The space-time evolution of the NOCE boundary expressed in terms of pressure altitudes contains a
 339 clear signal of the 11-year solar cycle in the 55°S-55°N range, which is suppressed mainly at high
 340 latitudes. The weak correlation of h_{eq}^y with $F_{10.7}$ index at high southern latitudes may be caused by the
 341 mentioned data gaps specified by the satellite sensing geometry. The same reason and distortions by
 342 SSWs evidently determine no correlation at high northern latitudes. Thus, at low and middle latitudes
 343 h_{eq}^y can be considered as a sensitive indicator of solar activity. Below, we present a simple and short
 344 explanation for this. Let us consider the NOCE criterion (9) at the pressure level p_{eq} :

$$VER(p_{eq}) = VER_{min}(T, M(p_{eq})).$$

345 In a zero approximation

$$346 \quad VER_{min} = 20 \cdot \frac{k_1 \cdot O_2(p_{eq}) \cdot M(p_{eq}) \cdot \left(k_4 \cdot O_2(p_{eq}) \cdot M(p_{eq}) \cdot \left(1 - \frac{k_5 + k_6}{k_3} \right) + k_2 \cdot O_3(p_{eq}) \right) \cdot A(T, M(p_{eq}))}{k_2} \cong$$

$$347 \quad 20 \cdot \frac{k_1 \cdot k_4 \cdot (O_2(p_{eq}) \cdot M(p_{eq}))^2 \cdot A(T, M(p_{eq}))}{k_2} \sim \frac{k_1 \cdot k_4 \cdot (p_{eq}/T)^4 \cdot A(T, p_{eq})}{k_2} \sim \frac{\exp(470/T) \cdot p_{eq}^4 \cdot A(T, p_{eq})}{T^{8.2}},$$

348

where $A(T, p_{eq}) =$

349

$$\frac{0.47 \cdot 118.35}{215.05 + 2.5 \cdot 10^{-11} \cdot O_2 / M \cdot \frac{p_{eq}}{k_B T} + 3.36 \cdot 10^{-13} \cdot e^{\frac{220}{T}} \cdot N_2 / M \cdot \frac{p_{eq}}{k_B T}} + \frac{0.34 \cdot 117.21}{178.06 + 4.8 \cdot 10^{-13} \cdot O_2 / M \cdot \frac{p_{eq}}{k_B T} + 7 \cdot 10^{-13} \cdot N_2 / M \cdot \frac{p_{eq}}{k_B T}} +$$

350

$$\frac{0.47 \cdot 117.21 \cdot (20.05 + 4.2 \cdot 10^{-12} \cdot O_2 / M \cdot \frac{p_{eq}}{k_B T} + 4 \cdot 10^{-13} \cdot N_2 / M \cdot \frac{p_{eq}}{k_B T})}{(215.05 + 2.5 \cdot 10^{-11} \cdot O_2 / M \cdot \frac{p_{eq}}{k_B T} + 3.36 \cdot 10^{-13} \cdot e^{\frac{220}{T}} \cdot N_2 / M \cdot \frac{p_{eq}}{k_B T}) \cdot (178.06 + 4.8 \cdot 10^{-13} \cdot O_2 / M \cdot \frac{p_{eq}}{k_B T} + 7 \cdot 10^{-13} \cdot N_2 / M \cdot \frac{p_{eq}}{k_B T})}.$$

351

Our analysis of $A(T, p_{eq})$ shows that this function can be approximately rewritten as $A(T, p_{eq}) \approx$

352

 $const + \frac{const}{const + \frac{p_{eq}}{T}}$. So, one can see that VER_{min} is strongly dependent on T . Moreover, it anticorrelates

353

with T . Gan et al. (2017) and Zhao et al. (2020) analyzed the simulated and measured data and revealed a

354

clear correlation between the MLT temperature above 80 km and the 10.7-cm solar radio flux. Moreover,

355

the dependence of the correlation coefficient of T with $F_{10.7}$ index on latitude in the 55°S-55°N range

356

given in Figure 9 in the paper by of Zhao et al. (2020) is consistent with our Figure 9 (left panel), taking

357

into account the sign of the correlation. Thus, we can conclude that the found anticorrelation of the NOCE

358

boundary h_{eq}^y with solar activity is caused by the strong connection with temperature, which, in turn, is

359

in a good correlation with the $F_{10.7}$ index. A detailed analysis of the reasons why the solar cycle weakly

360

manifests itself in the spatio-temporal variability of z_{eq}^y is not so simple and is beyond the scope of this

361

work.

362

Figure 5 illustrates an interesting peculiarity. At middle latitudes, the summer h_{eq}^m and z_{eq}^m are

363

remarkably (by several kilometers) higher than the winter ones, while the opposite relationship could be

364

expected. Due to more effective daytime HO_x photoproduction at these altitudes, the summer H values at

365

the beginning of the night are higher than the ones in winter. So, the summer ozone lifetimes should be

366

shorter and the NOCE condition is more favourable than in winter. Nevertheless, the same ratio between

367

the summer and winter NOCE boundaries at middle latitudes was revealed in Belikovich et al. (2018) and

368

Kulikov et al. (2018a), where the boundary of this equilibrium was determined by direct comparison of

369

 O_3 and O_3^{eq} concentrations from results of 3D chemical-transport models. Based on the results of Section

370

3, we can assume that the discussed effect is connected with the height position of the transition zone,

371

which demonstrates the same variation (see Figures 1-3). Kulikov et al. (2023) derived the equations

372

describing pure chemical O and H nighttime evolution:

373

$$\begin{cases} \frac{dO}{dt} = -2 \cdot k_4 \cdot M \cdot O_2 \cdot H - 2 \cdot k_2 \cdot H \cdot O_3 \\ \frac{dH}{dt} = -2 \cdot k_4 \cdot M \cdot O_2 \cdot \frac{k_5 + k_6}{k_3} \cdot \frac{H^2}{O} \end{cases} \quad (12)$$

374

Neglecting the second term in the first equation as a secondary one, this system can be solved

375

analytically, so that the nighttime evolution times of O and H are:

$$376 \quad \tau_O \equiv \frac{O}{|dO/dt|} = \frac{1}{2 \cdot k_4 \cdot M \cdot O_2} \cdot \left(\frac{O}{H}\right)_{t=t_{bn}} - \left(1 - \frac{k_5 + k_6}{k_3}\right) \cdot (t - t_{bn}), \quad (13)$$

$$377 \quad \tau_H \equiv \frac{H}{|dH/dt|} = \frac{1}{2 \cdot k_4 \cdot M \cdot O_2} \cdot \frac{k_3}{k_5 + k_6} \cdot \left(\frac{O}{H}\right)_{t=t_{bn}} - \left(\frac{k_3}{k_5 + k_6} - 1\right) \cdot (t - t_{bn}), \quad (14)$$

378 where t_{bn} is the time of the beginning of the night, $\left(\frac{O}{H}\right)_{t=t_{bn}}$ is the O/H ratio at the beginning of the
 379 night. Note that k_3 is much larger than $k_5 + k_6$ (see Table 1). Based on the daytime O and H distributions
 380 in the mesopause region obtained in Kulikov et al. (2022), we calculated the ratio of the summer O/H to
 381 the winter O/H (see Figure 14). During the summer, O/H at middle latitudes is remarkably less than in
 382 winter in both, northern and southern hemispheres, whereas the air concentration and the rate of reaction
 383 R4 (see Table 1) increase due to a decrease in temperature. As a result, the summer τ_O and τ_H are
 384 essentially shorter than their winter values, which explains the summer rise of the transition zone and the
 385 NOCE boundary.

386 Finally, let us briefly discuss other qualitative indicators of the NOCE boundary, which could be
 387 found in the SABER database. As mentioned above, Kulikov et al. (2019) showed that the nighttime O
 388 SABER profiles are correct above the NOCE boundary, whereas the H profiles hold within the whole
 389 pressure interval. Kulikov et al. (2021) demonstrated that, in the altitude range of 80-85 km, many H
 390 profiles have a sharp jump in concentration when it increases from $\sim 10^7 \text{ cm}^{-3}$ to $\sim 10^8 \text{ cm}^{-3}$. Our analysis
 391 with the criterion (9) shows that the altitude of these jumps can be used as a rough indicator of the NOCE
 392 boundary.

393

394 **7 Conclusions**

395 The NOCE criterion is not only a useful technical characteristic for the retrieval of O from satellite
 396 data, but it also reproduces the transition zone position which separates deep and weak diurnal
 397 oscillations of O and H at low and middle latitudes. At middle latitudes, the summer boundary of NOCE
 398 is remarkably (by several kilometers) higher than the winter one, which is accompanied with the same
 399 variation of the transition zone. This effect is explained by the markedly lower values of the O and H
 400 nighttime evolution times in summer than in winter by virtue of the lower values of the O/H ratio at the
 401 beginning of the night and air concentration increase.

402 The NOCE boundary according to the criterion is sensitive to sporadic abrupt changes in the
 403 dynamics of the middle atmosphere.

404 The NOCE boundary at low and middle latitudes expressed in pressure altitudes contains a clear
 405 signal of 11-year solar cycle and can be considered as a sensitive indicator of solar activity.

406

407 **Data availability.** The SABER data are obtained from the website (<https://saber.gats-inc.com>). The data
408 of solar radio flux at 10.7 cm in 2002-2021 were downloaded from
409 http://www.wdcb.ru/stp/solar/solar_flux.ru.html and [https://www.spaceweather.gc.ca/forecast-
410 prevision/solar-solaire/solarflux/sx-5-en.php](https://www.spaceweather.gc.ca/forecast-
410 prevision/solar-solaire/solarflux/sx-5-en.php).

411

412 **Code availability.** Code is available upon request.

413

414 **Author contributions.** MK and MB performed data processing and analysis and wrote the manuscript.
415 AC, SD, and AM contributed to reviewing the article.

416

417 **Competing interests.** The authors declare that they have no conflict of interest.

418

419 **Acknowledgements.** The authors are grateful to the SABER team for data availability.

420

421 **Financial support.** The main results presented in Sections 3 and 5 were obtained under the support by
422 the Russian Science Foundation under grant No. 22-12-00064 (<https://rscf.ru/project/22-12-00064/>). The
423 analysis of the difference between the NOCE boundary in summer and winter at middle latitudes and the
424 reasons of well anticorrelation of the NOCE boundary with $F_{10.7}$ index were carried out at the expense of
425 state assignment no. 0729-2020-0037.

426

427 **References**

428 Allen, M., Lunine, J. I., and Yung, Y. L.: The vertical distribution of ozone in the mesosphere and lower
429 thermosphere, *J. Geophys. Res.*, 89(D3), 4841–4872, <https://doi.org/10.1029/JD089iD03p04841>, 1984.
430 Belikovich, M. V., Kulikov, M. Yu, Grygalashvyly, M., Sonnemann, G. R., Ermakova, T. S., Nechaev,
431 A. A., and Feigin, A .M.: Ozone chemical equilibrium in the extended mesopause under the nighttime
432 conditions, *Adv. Space Res.*, 61, 426–432, <https://doi.org/10.1016/j.asr.2017.10.010>, 2018.
433 Burkholder, J. B., Sander, S. P., Abbatt, J., Barker, J. R., Cappa, C., Crouse, J. D., Dibble, T. S., Huie,
434 R. E., Kolb, C. E., Kurylo, M. J., Orkin, V. L., Percival, C. J., Wilmouth, D. M., and Wine, P. H.:

435 Chemical Kinetics and Photochemical Data for Use in Atmospheric Studies, Evaluation No. 19, JPL
436 Publication 19-5, Jet Propulsion Laboratory, Pasadena, <http://jpldataeval.jpl.nasa.gov>, 2020.

437 Evans, W. F. J., McDade, I. C., Yuen, J., and Llewellyn, E. J.: A rocket measurement of the O₂ infrared
438 atmospheric (0-0) band emission in the dayglow and a determination of the mesospheric ozone and
439 atomic oxygen densities, *Can. J. Phys.*, 66, 941–946, <https://doi.org/10.1139/p88-151>. 1988.

440 Gan, Q., Du, J., Fomichev, V. I., Ward, W. E., Beagley, S. R., Zhang, S., and Yue, J.: Temperature
441 responses to the 11 year solar cycle in the mesosphere from the 31 year (1979–2010) extended Canadian
442 Middle Atmosphere Model simulations and a comparison with the 14 year (2002–2015) TIMED/SABER
443 observations, *J. Geophys. Res. Space Physics*, 122, 4801–4818, <https://doi.org/10.1002/2016JA023564>,
444 2017.

445 García-Comas, M., Funke, B., López-Puertas, M., González-Galindo, F., Kiefer, M., and Höpfner, M.:
446 First detection of a brief mesoscale elevated stratopause in very early winter. *Geophys. Res. Lett.*, 47,
447 e2019GL086751, <https://doi.org/10.1029/2019GL086751>, 2020.

448 Good, R. E.: Determination of atomic oxygen density from rocket borne measurements of hydroxyl
449 airglow, *Planet. Space Sci.*, 24, 389–395, [https://doi.org/10.1016/0032-0633\(76\)90052-0](https://doi.org/10.1016/0032-0633(76)90052-0), 1976.

450 Grygalashvyly, M., Sonnemann, G. R., and Hartogh, P.: Long-term behavior of the concentration of the
451 minor constituents in the mesosphere - A model study, *Atmos. Chem. Phys.*, 9, 2779–2792,
452 <https://doi.org/10.5194/acp-9-2779-2009>, 2009.

453 Grygalashvyly, M., Sonnemann, G. R., Lübken, F.-J., Hartogh, P., and Berger, U.: Hydroxyl layer: Mean
454 state and trends at midlatitudes, *J. Geophys. Res. Atmos.*, 119, 12,391–12,419,
455 <https://doi.org/10.1002/2014JD022094>, 2014.

456 Grygalashvyly, M.: Several notes on the OH* layer, *Ann. Geophys.*, 33, 923-930,
457 <https://doi.org/10.5194/angeo-33-923-2015>, 2015.

458 Hartogh, P., Jarchow, C., Sonnemann, G. R., and Grygalashvyly, M.: On the spatiotemporal behavior of
459 ozone within the upper mesosphere/mesopause region under nearly polar night conditions, *J. Geophys.*
460 *Res.*, 109, D18303, <https://doi.org/10.1029/2004JD004576>, 2004.

461 Hartogh, P., Jarchow, Ch., Sonnemann, G. R., and Grygalashvyly, M.: Ozone distribution in the middle
462 latitude mesosphere as derived from microwave measurements at Lindau (51.66°N, 10.13°E), *J. Geophys.*
463 *Res.*, 116, D04305, <https://doi.org/10.1029/2010JD014393>, 2011.

464 Feigin, A. M., Konovalov, I. B., and Molkov, Y. I.: Towards understanding nonlinear nature of
465 atmospheric photochemistry: Essential dynamic model of the mesospheric photochemical system., *J.*
466 *Geophys. Res.: Atmos.*, 103, 25,447–25,460, <https://doi.org/10.1029/98JD01569>, 1998.

467 Konovalov, I. B., and Feigin, A. M.: Towards an understanding of the non-linear nature of atmospheric
468 photochemistry: origin of the complicated dynamic behavior of the mesospheric photochemical system,
469 *Nonlin. Processes Geophys.*, 87-104, <https://doi.org/10.5194/npg-7-87-2000>, 2000.

470 Körner, U., and Sonnemann, G. R.: Global 3D-modeling of water vapor concentration of the
471 mesosphere/mesopause region and implications with respect to the NLC region, *J. Geophys. Res.*, 106,
472 9639– 9651, <https://doi.org/10.1029/2000JD900744>, 2001.

473 Kowalewski, S., v. Savigny, C., Palm, M., McDade, I. C., and Notholt, J.: On the impact of the temporal
474 variability of the collisional quenching process on the mesospheric OH emission layer: a study based on
475 SD-WACCM4 and SABER, *Atmos. Chem. Phys.*, 14, 10193-10210, [https://doi.org/10.5194/acp-14-](https://doi.org/10.5194/acp-14-10193-2014)
476 10193-2014, 2014.

477 Kremp, C., Berger, U., Hoffmann, P., Keuer, D., and Sonnemann, G. R.: Seasonal variation of middle
478 latitude wind fields of the mesopause region—A comparison between observation and model calculation,
479 *Geophys. Res. Lett.*, 26, 1279–1282, <https://doi.org/10.1029/1999GL900218>, 1999.

480 Kulikov, M. Yu., and Feigin, A. M.: Reactive-diffusion waves in the mesospheric photochemical system.
481 *Adv. Space Res.*, 35(11), 1992-1998, <https://doi.org/10.1016/j.asr.2005.04.020>, 2005.

482 Kulikov, M. Yu.: Theoretical investigation of the influence of a quasi 2-day wave on nonlinear
483 photochemical oscillations in the mesopause region, *J. Geophys. Res.*, 112, D02305,
484 <https://doi.org/10.1029/2005JD006845>, 2007.

485 Kulikov, M. Y., Belikovich, M. V., Grygalashvyly, M., Sonnemann, G. R., Ermakova, T. S., Nechaev, A.
486 A., and Feigin, A. M.: Daytime ozone loss term in the mesopause region, *Ann. Geophys.*, 35, 677-682
487 <https://doi.org/10.5194/angeo-35-677-2017>, 2017.

488 Kulikov, M. Y., Belikovich, M. V., Grygalashvyly, M., Sonnemann, G. R., Ermakova, T. S., Nechaev, A.
489 A., and Feigin, A. M.: Nighttime ozone chemical equilibrium in the mesopause region. *J. Geophys.*
490 *Res.*, 123, 3228–3242, <https://doi.org/10.1002/2017JD026717>, 2018a.

491 Kulikov, M. Y., Nechaev, A. A., Belikovich, M. V., Ermakova, T. S., and Feigin, A. M.: Technical note:
492 Evaluation of the simultaneous measurements of mesospheric OH, HO₂, and O₃ under a photochemical
493 equilibrium assumption – a statistical approach, *Atm. Chem. Phys.*, 18, 7453-747,
494 <https://doi.org/10.5194/acp-18-7453-2018>, 2018b.

495 Kulikov, M. Yu., Nechaev, A. A., Belikovich, M. V., Vorobeva, E. V., Grygalashvyly, M., Sonnemann,
496 G. R., and Feigin, A. M.: Border of nighttime ozone chemical equilibrium in the mesopause region from
497 saber data: implications for derivation of atomic oxygen and atomic hydrogen, *Geophys. Res. Lett.*, 46,
498 997– 1004, <https://doi.org/10.1029/2018GL080364>, 2019.

499 Kulikov, M. Y., Belikovich, M. V., and Feigin, A. M.: Analytical investigation of the reaction-diffusion
500 waves in the mesopause photochemistry, *J. Geophys. Res.*, 125, e2020JD033480,
501 <https://doi.org/10.1029/2020JD033480>, 2020.

502 Kulikov, M. Y., Belikovich, M. V., Feigin, A. M.: The 2-day photochemical oscillations in the mesopause
503 region: the first experimental evidence? *Geophys. Res. Lett.*, 48, e2021GL092795,
504 <https://doi.org/10.1029/2021GL092795>, 2021.

505 Kulikov, M. Y., Belikovich, M. V., Grygalashvyly, M., Sonnemann, G. R., and Feigin, A.M.: The revised
506 method for retrieving daytime distributions of atomic oxygen and odd-hydrogens in the mesopause region
507 from satellite observations, *Earth Planets Space*, 74, 44, <https://doi.org/10.1186/s40623-022-01603-8>,
508 2022.

509 Kulikov, M. Yu., Belikovich, M. V., Chubarov, A. G., Dementeyva, S. O., Feigin, A. M.: Boundary of
510 nighttime ozone chemical equilibrium in the mesopause region: improved criterion of determining the
511 boundary from satellite data, *Adv. Space Res.*, 71 (6), 2770-2780,
512 <https://doi.org/10.1016/j.asr.2022.11.005>, 2023.

513 Llewellyn, E. J., McDade, I. C. Moorhouse, P. and Lockerbie M. D.: Possible reference models for
514 atomic oxygen in the terrestrial atmosphere, *Adv. Space Res.*, 13, 135–144, [https://doi.org/10.1016/0273-1177\(93\)90013-2](https://doi.org/10.1016/0273-1177(93)90013-2), 1993.

516 Llewellyn, E. J., and McDade, I. C.: A reference model for atomic oxygen in the terrestrial atmosphere,
517 *Adv. Space Res.*, 18, 209–226, [https://doi.org/10.1016/0273-1177\(96\)00059-2](https://doi.org/10.1016/0273-1177(96)00059-2), 1996.

518 Lübken, F.-J., Berger, U. and Baumgarten, G.: Temperature trends in the midlatitude summer
519 mesosphere, *J. Geophys. Res. Atmos.*, 118, 13347–13360, <https://doi.org/10.1002/2013JD020576>, 2013.

520 Manney, G. L., Kruger, K., Sabutis, J. L., Sena, S. A., and Pawson, S.: The remarkable 2003–2004 winter
521 and other recent warm winters in the Arctic stratosphere since the late 1990s. *J. Geophys. Res.*, 110,
522 D04107, <https://doi.org/10.1029/2004JD005367>, 2005.

523 Marsh, D. R., Smith, A. K., Mlynczak, M. G., and Russell III, J. M.: SABER observations of the OH
524 Meinel airglow variability near the mesopause, *J. Geophys. Res.*, 111, A10S05,
525 <https://doi.org/10.1029/2005JA011451>, 2006.

526 McDade, I. C., Llewellyn, E. J., and Harris, F. R.: Atomic oxygen concentrations in the lower auroral
527 thermosphere, *Adv. Space Res.*, 5, 229–232, <https://doi.org/10.1029/GL011I003P00247>, 1985.

528 McDade, I. C., and Llewellyn, E. J.: Mesospheric oxygen atom densities inferred from night-time OH
529 Meinel band emission rates, *Planet. Space Sci.*, 36, 897–905, [https://doi.org/10.1016/0032-0633\(88\)90097-9](https://doi.org/10.1016/0032-0633(88)90097-9), 1988.

531 Mlynczak, M. G., Marshall, B. T., Martin-Torres, F. J., Russell III, J. M., Thompson, R. E., Remsberg, E.
532 E., and Gordley, L. L.: Sounding of the Atmosphere using Broadband Emission Radiometry observations
533 of daytime mesospheric O₂(¹D) 1.27 μm emission and derivation of ozone, atomic oxygen, and solar and
534 chemical energy deposition rates, *J. Geophys. Res.*, 112, D15306, <https://doi.org/10.1029/2006JD008355>,
535 2007.

536 Mlynczak, M. G., Hunt, L. A., Mast, J. C., Marshall, B. T., Russell III, J. M., Smith, A. K., Siskind, D. E.,
537 Yee, J.-H., Mertens, C. J., Martin-Torres, F. J., Thompson, R. E., Drob, D. P., and Gordley, L. L.: Atomic
538 oxygen in the mesosphere and lower thermosphere derived from SABER: Algorithm theoretical basis and
539 measurement uncertainty, *J. Geophys. Res.*, 118, 5724–5735, <https://doi.org/10.1002/jgrd.50401>, 2013a.

540 Mlynczak, M. G., Hunt, L. H., Mertens, C. J., Marshall, B. T., Russell III, J. M., López-Puertas, M.,
541 Smith, A. K., Siskind, D. E., Mast, J. C., Thompson, R. E., and Gordley, L. L.: Radiative and energetic
542 constraints on the global annual mean atomic oxygen concentration in the mesopause region, *J. Geophys.*
543 *Res. Atmos.*, 118, 5796–5802, <https://doi.org/10.1002/jgrd.50400>, 2013b.

544 Mlynczak, M. G., Hunt, L. A. Marshall, B. T. Mertens, C. J. Marsh, D. R. Smith, A. K. Russell, J. M.
545 Siskind D. E., and Gordley L. L.: Atomic hydrogen in the mesopause region derived from SABER:
546 Algorithm theoretical basis, measurement uncertainty, and results, *J. Geophys. Res.*, 119, 3516–3526,
547 <https://doi.org/10.1002/2013JD021263>, 2014.

548 Mlynczak, M. G., Hunt, L. A., Russell, J. M. III, and Marshall, B. T.: Updated SABER night atomic
549 oxygen and implications for SABER ozone and atomic hydrogen, *Geophys. Res. Lett.*, 45, 5735–5741,
550 <https://doi.org/10.1029/2018GL077377>, 2018.

551 Morton, K. W., and Mayers, D. F.: *Numerical Solution of Partial Differential Equations*, Cambridge
552 University Press, 1994.

553 Nikoukar, R., Swenson, G. R., Liu, A. Z., and Kamalabadi, F.: On the variability of mesospheric OH
554 emission profiles, *J. Geophys. Res.*, 112, D19109, <https://doi.org/10.1029/2007JD008601>, 2007.

555 Panka, P. A., Kutepov, A. A., Rezac, L., Kalogerakis, K. S., Feofilov, A. G., Marsh, D., Janches, D., and
556 Yiğit, E. Atomic oxygen retrieved from the SABER 2.0- and 1.6- μ m radiances using new first-principles
557 nighttime OH(v) model, *Geophys. Res. Lett.*, 45, 5798–5803, <https://doi.org/10.1029/2018GL077677>,
558 2018.

559 Pendleton, W. R., Baker, K. D., Howlett, L. C.: Rocket-based investigations of O(³P), O₂ (a¹ Δ_g) and OH*
560 (v=1,2) during the solar eclipse of 26 February 1979, *J. Atm. Terr. Phys.*, 45(7), 479-491, 1983.

561 Siskind, D. E., Marsh, D. R., Mlynczak, M. G., Martin-Torres, F. J., and Russell III, J. M.: Decreases in
562 atomic hydrogen over the summer pole: Evidence for dehydration from polar mesospheric clouds?
563 *Geophys. Res. Lett.*, 35, L13809, <https://doi.org/10.1029/2008GL033742>, 2008.

564 Siskind, D. E., Mlynczak, M. G., Marshall, T., Friedrich, M., Gumbel, J.: Implications of odd oxygen
565 observations by the TIMED/SABER instrument for lower D region ionospheric modeling, *J. Atmos. Sol.*
566 *Terr. Phys.*, 124, 63–70, <https://doi.org/10.1016/j.jastp.2015.01.014>, 2015.

567 Schmidlin, F. J.: First observation of mesopause temperature lower than 100 K, *Geophys. Res. Lett.*, 19,
568 1643-1646, <https://doi.org/10.1029/92GL01506>, 1992.

569 Shimazaki, T.: *Minor Constituents in the Middle Atmosphere*, D. Reidel, Norwell, Mass., USA, 444 pp.,
570 1985.

571 Smith, A. K., Lopez-Puertas, M., Garcia-Comas, M. and Tukiainen, S.: SABER observations of
572 mesospheric ozone during NH late winter 2002–2009, *Geophys. Res. Lett.*, 36, L23804,
573 <https://doi.org/10.1029/2009GL040942>, 2009.

574 Smith, A. K., Marsh, D. R. Mlynczak, M. G. and Mast, J. C.: Temporal variations of atomic oxygen in the
575 upper mesosphere from SABER, *J. Geophys. Res.*, 115, D18309, <https://doi.org/10.1029/2009JD013434>,
576 2010.

577 Sonnemann, G., and Fichtelmann, B.: Enforced oscillations and resonances due to internal non-linear
578 processes of photochemical system in the atmosphere, *Acta. Geod. Geophys. Mont. Hung.*, 22, 301–311,
579 1987.

580 Sonnemann, G., and Fichtelmann, B.: Subharmonics, cascades of period of doubling and chaotic behavior
581 of photochemistry of the mesopause region, *J. Geophys. Res.*, 101, 1193-1203,
582 <https://doi.org/10.1029/96JD02740>, 1997.

583 Sonnemann, G., Kremp, C. Ebel, A. and Berger U.: A three-dimensional dynamic model of minor
584 constituents of the mesosphere, *Atmos. Environ.*, 32, 3157–3172, <https://doi.org/10.1016/S1352->
585 2310(98)00113-7, 1998.

586 Sonnemann, G., Feigin, A. M., and Molkov, Ya. I.: On the influence of diffusion upon the nonlinear
587 behaviour of the photochemistry of the mesopause region, *J. Geophys. Res.*, 104, 30591-30603,
588 <https://doi.org/10.1029/1999JD900785>, 1999.

589 Sonnemann, G., and Feigin, A. M.: Non-linear behaviour of a reaction-diffusion system of the
590 photochemistry within the mesopause region, *Phys. Rev. E*, 59, 1719-1726,
591 <https://doi.org/10.1103/PhysRevE.59.1719>, 1999.

592 Sonnemann, G. R.: The photochemical effects of dynamically induced variations in solar insolation, *J.*
593 *Atmos. Sol. Terr. Phys.*, 63, 781-797, [https://doi.org/10.1016/S1364-6826\(01\)00010-4](https://doi.org/10.1016/S1364-6826(01)00010-4), 2001.

594 Sonnemann, G. R., and Grygalashvyly, M.: On the two-day oscillations and the day-to-day variability in
595 global 3-D-modeling of the chemical system of the upper mesosphere/mesopause region, *Nonlin.*
596 *Processes Geophys.*, 12, 691– 705, <https://doi.org/10.5194/npg-12-691-2005>, 2005.

597 Sonnemann, G. R., Hartogh, P., Berger, U., and Grygalashvyly, M.: Hydroxyl layer: trend of number
598 density and intra-annual variability, *Ann. Geophys.*, 33, 749–767, <https://doi.org/10.5194/angeo-33-749->
599 2015, 2015.

600 Swenson, G. R., and Gardner C. S.: Analytical models for the responses of the mesospheric OH* and Na
601 layers to atmospheric gravity waves, *J. Geophys. Res.*, 103(D6), 6271–6294,
602 <https://doi.org/10.1029/97JD02985>, 1998.

603 Thomas, G. E., Olivero, J. J., Jensen, E. J., Schroder, W., and Toon, O. B.: Relation between increasing
604 methane and the presence of ice clouds at the mesopause, *Nature*, 338, 490–
605 492 <https://doi.org/10.1038/338490a0>, 1989.

606 Thomas, R. J.: Atomic hydrogen and atomic oxygen density in the mesosphere region: Global and
607 seasonal variations deduced from Solar Mesosphere Explorer near-infrared emissions, *J. Geophys. Res.*,
608 95, 16,457–16,476, <https://doi.org/10.1029/JD095iD10p16457>, 1990.

609 Thomas, G. E.: Mesospheric clouds and the physics of the mesopause region, *Rev. Geophys.*, 29, 553–
610 575, <https://doi.org/10.1029/91RG01604>, 1991.

611 Walcek, C. J.: Minor flux adjustment near mixing ratio extremes for simplified yet highly accurate
612 monotonic calculation of tracer advection, *J. Geophys. Res.*, 105, 9335-9348,
613 <https://doi.org/10.1029/1999JD901142>, 2000.

614 Xu, J., Smith, A. K., Jiang, G., Gao, H., Wei, Y., Mlynczak, M. G., and Russell III, J. M.: Strong
615 longitudinal variations in the OH nightglow, *Geophys. Res. Lett.*, 37, L21801,
616 <https://doi.org/10.1029/2010GL043972>, 2010.

617 Xu, J., Gao, H. Smith, A. K. and Zhu Y.: Using TIMED/SABER nightglow observations to investigate
618 hydroxyl emission mechanisms in the mesopause region, *J. Geophys. Res.*, 117, D02301,
619 <https://doi.org/10.1029/2011JD016342>, 2012.

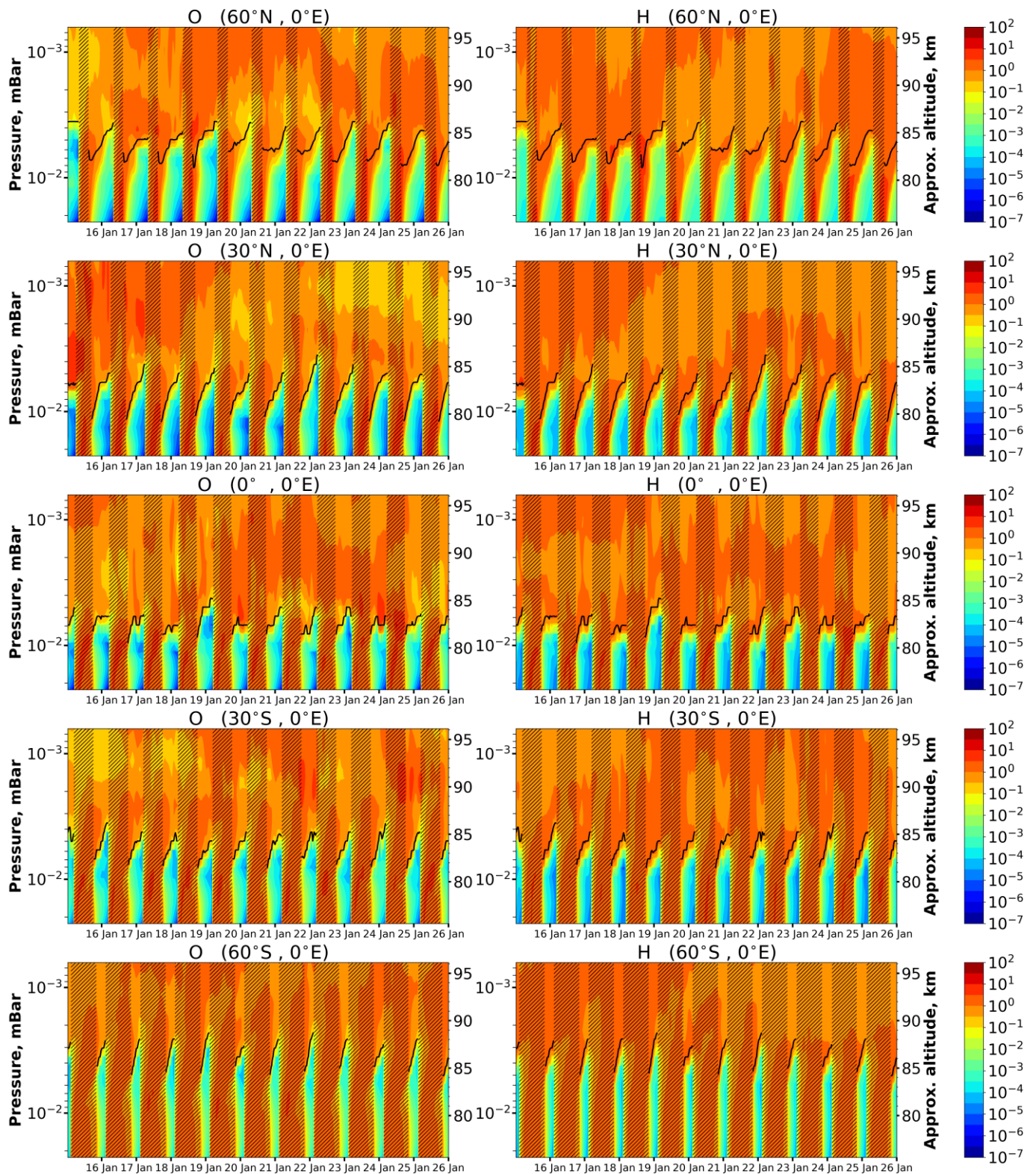
620 Zhao, X. R., Sheng, Z. Shi, H. Q. Weng, L. B. and He Y.: Middle Atmosphere Temperature Changes
621 Derived from SABER Observations during 2002–20, *J. Climate*, 34, 7995–8012,
622 <https://doi.org/10.1175/JCLI-D-20-1010.1>, 2021.

623 **Table 1.** List of reactions with corresponding reaction rates (for three-body reactions [$\text{cm}^6 \text{ molecule}^{-2}$
624 s^{-1}], for two-body reactions [$\text{cm}^3 \text{ molecule}^{-1} \text{ s}^{-1}$]) taken from Burkholder et al. (2020).

	Reaction	Rate constant
R1	$\text{O} + \text{O}_2 + \text{M} \rightarrow \text{O}_3 + \text{M}$	$k_1 = 6.1 \cdot 10^{-34} (298/T)^{2.4}$
R2	$\text{H} + \text{O}_3 \rightarrow \text{O}_2 + \text{OH}$	$k_2 = 1.4 \cdot 10^{-10} \exp(-470/T)$
R3	$\text{O} + \text{HO}_2 \rightarrow \text{O}_2 + \text{OH}$	$k_3 = 3 \cdot 10^{-11} \exp(200/T)$
R4	$\text{H} + \text{O}_2 + \text{M} \rightarrow \text{HO}_2 + \text{M}$	$k_4 = 5.3 \cdot 10^{-32} (298/T)^{1.8}$
R5	$\text{H} + \text{HO}_2 \rightarrow \text{O}_2 + \text{H}_2$	$k_5 = 6.9 \cdot 10^{-12}$
R6	$\text{H} + \text{HO}_2 \rightarrow \text{O} + \text{H}_2\text{O}$	$k_6 = 1.6 \cdot 10^{-12}$

625

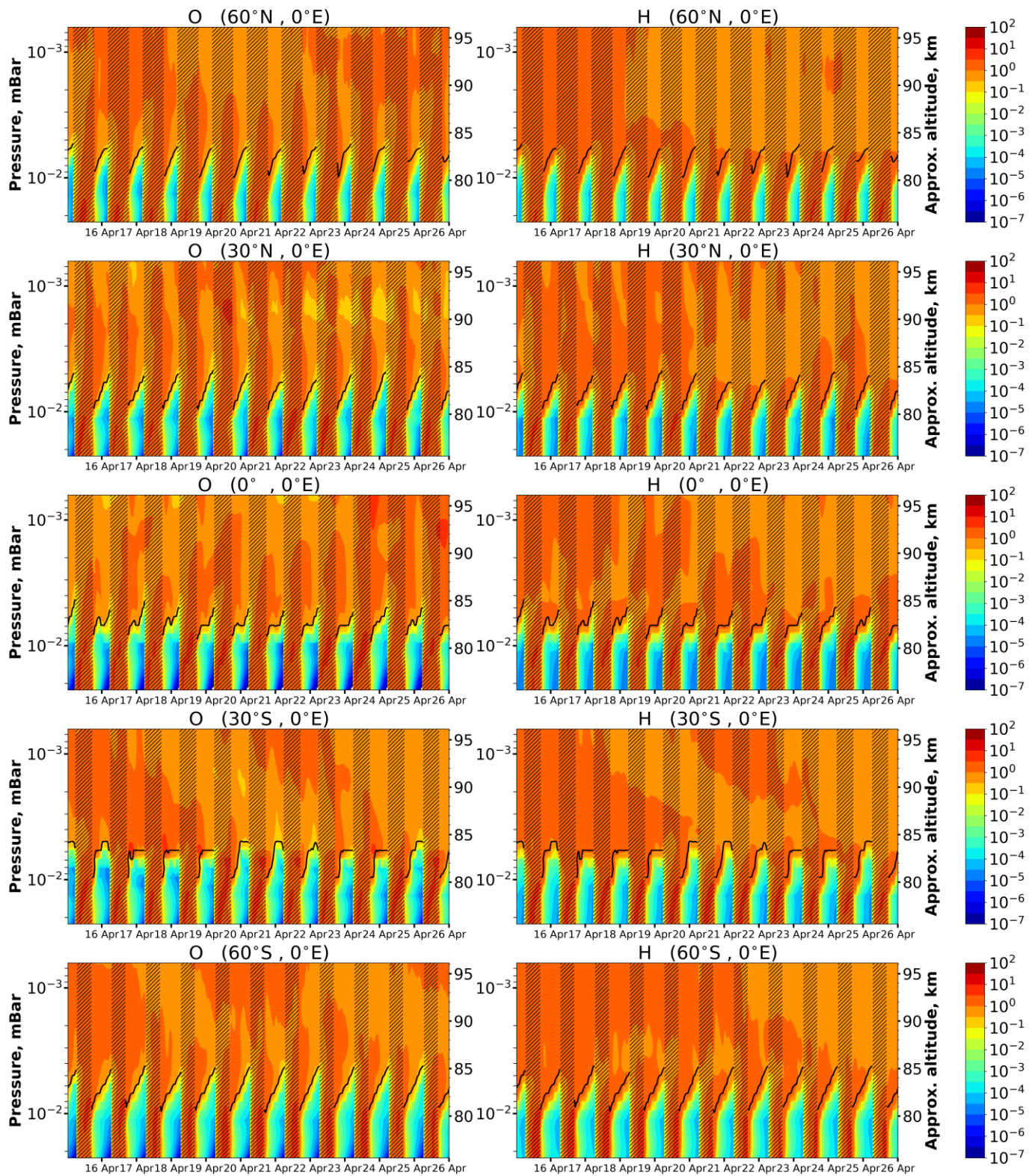
626



627

628 Figure 1. O and H time-height variations above different points in January 2000 calculated by 3D
 629 chemical transport model of middle atmosphere. Concentrations are normalized by mean daily values,
 630 correspondingly, calculated as a function of altitude. Dark bars mark daytime, light bars mark nighttime.
 631 Black lines point the NOCE boundary altitude in accordance to criterion (5) ($Cr = 0.1$).

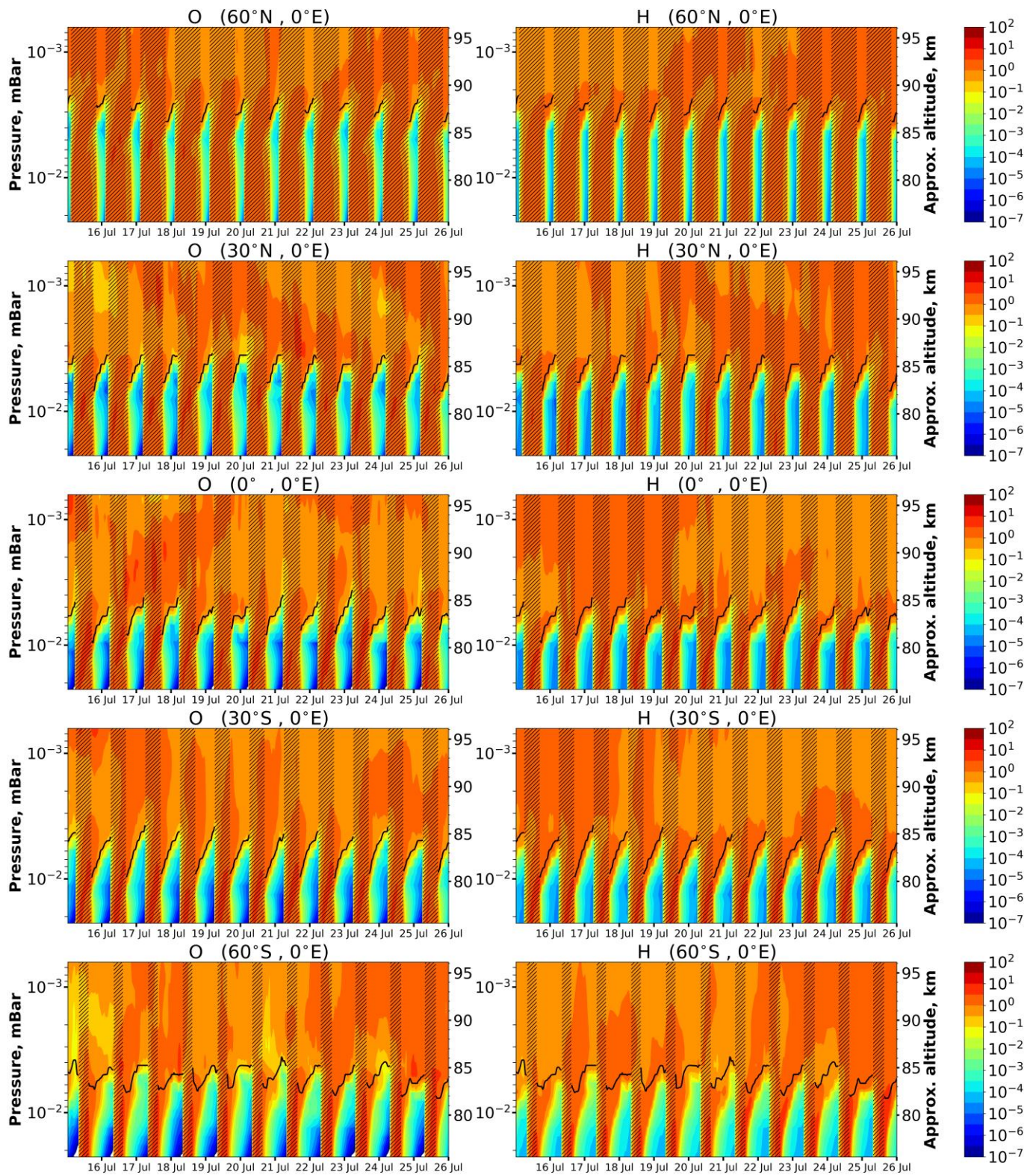
632



633

634 Figure 2. The same as in Fig. 1, but in April 2000. Black lines point NOCE boundary altitude according
 635 to criterion (5) ($Cr = 0.1$).

636

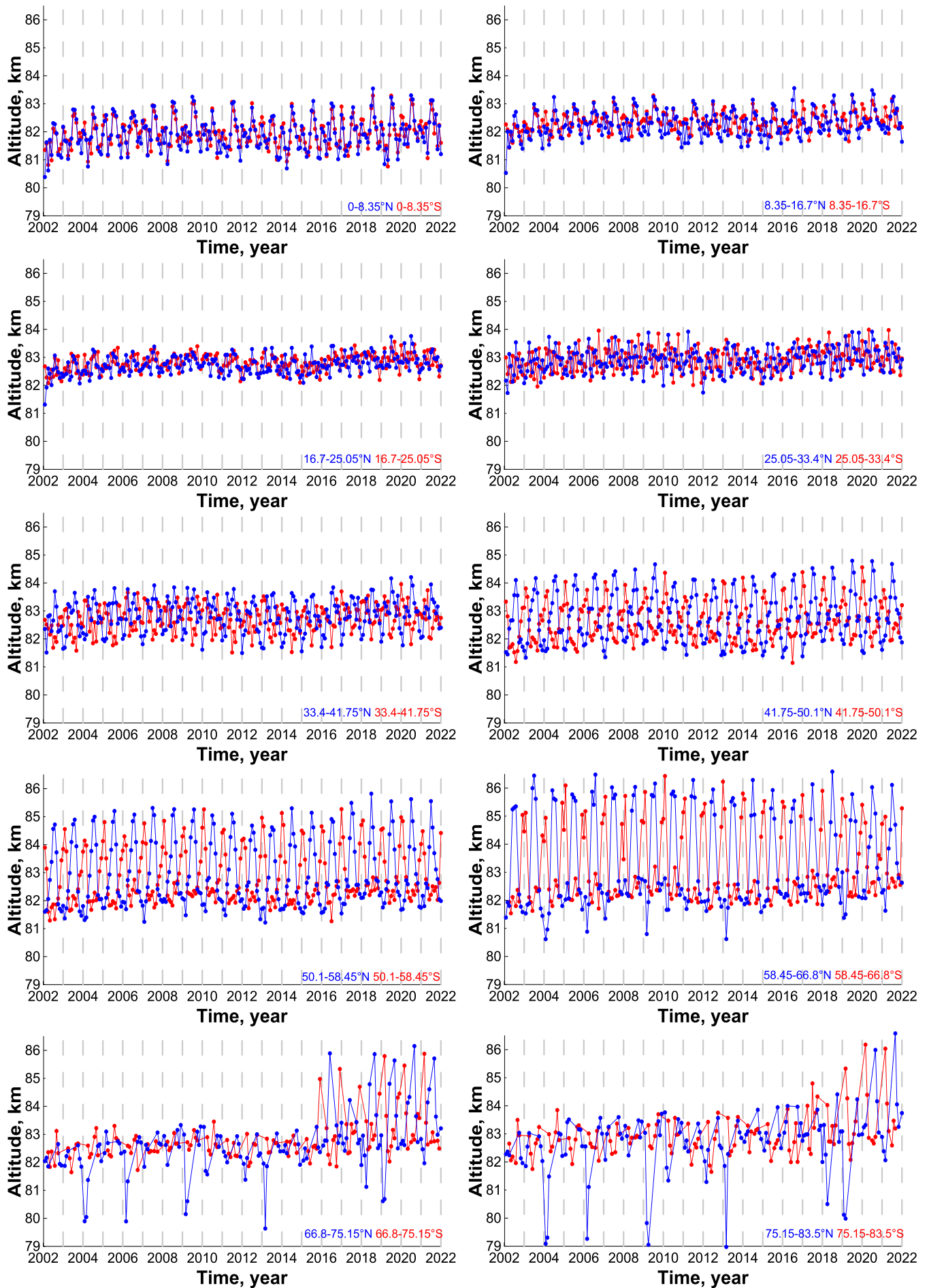


637

638 Figure 3. The same as in Fig. 1, but in July 2000. Black lines point the NOCE boundary altitude

639 according to criterion (5) ($Cr = 0.1$).

640



641

642

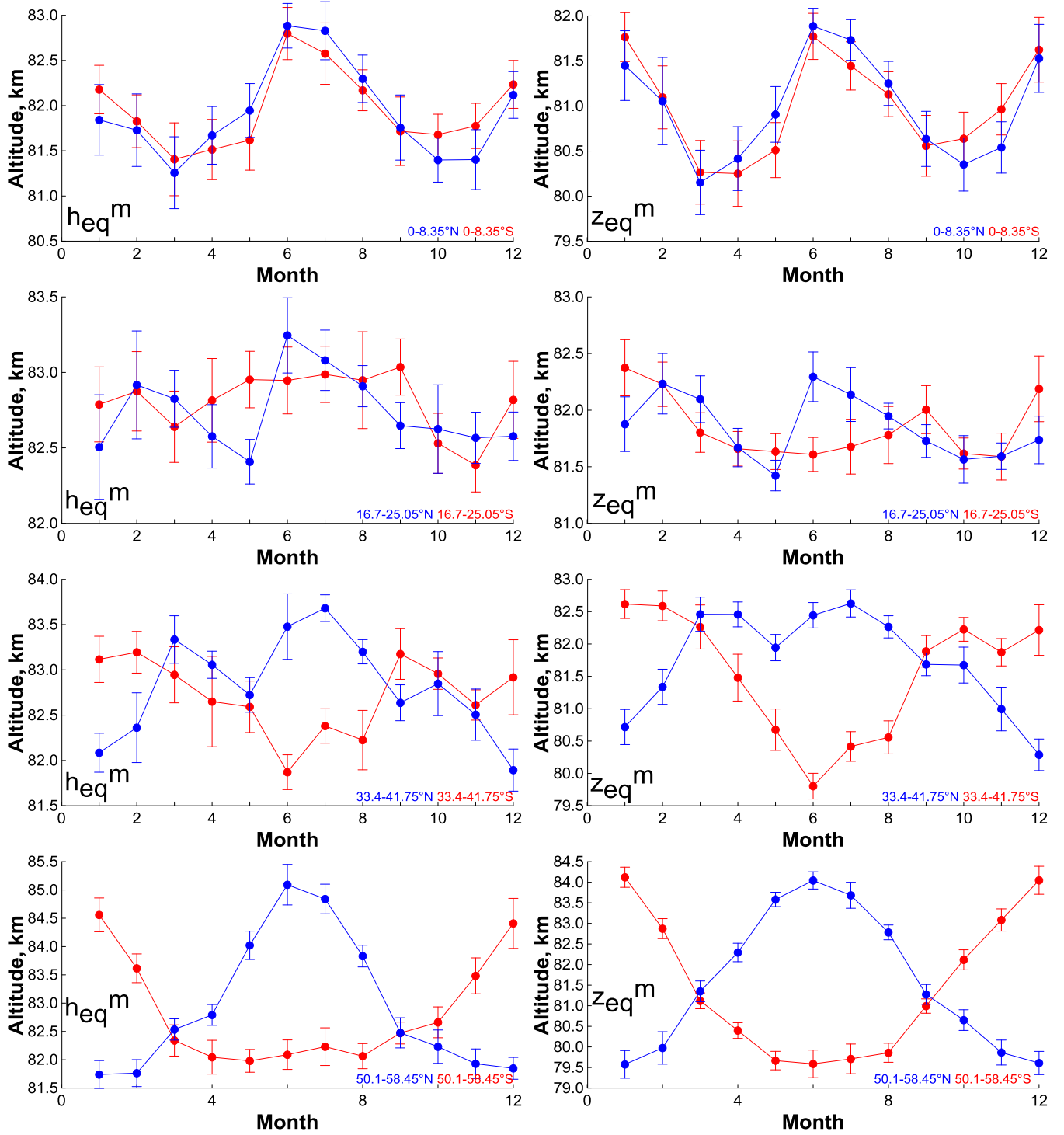
643

644

645

646

Figure 4. Time evolution of monthly mean pressure altitude h_{eq}^m at different latitudes.



647

648

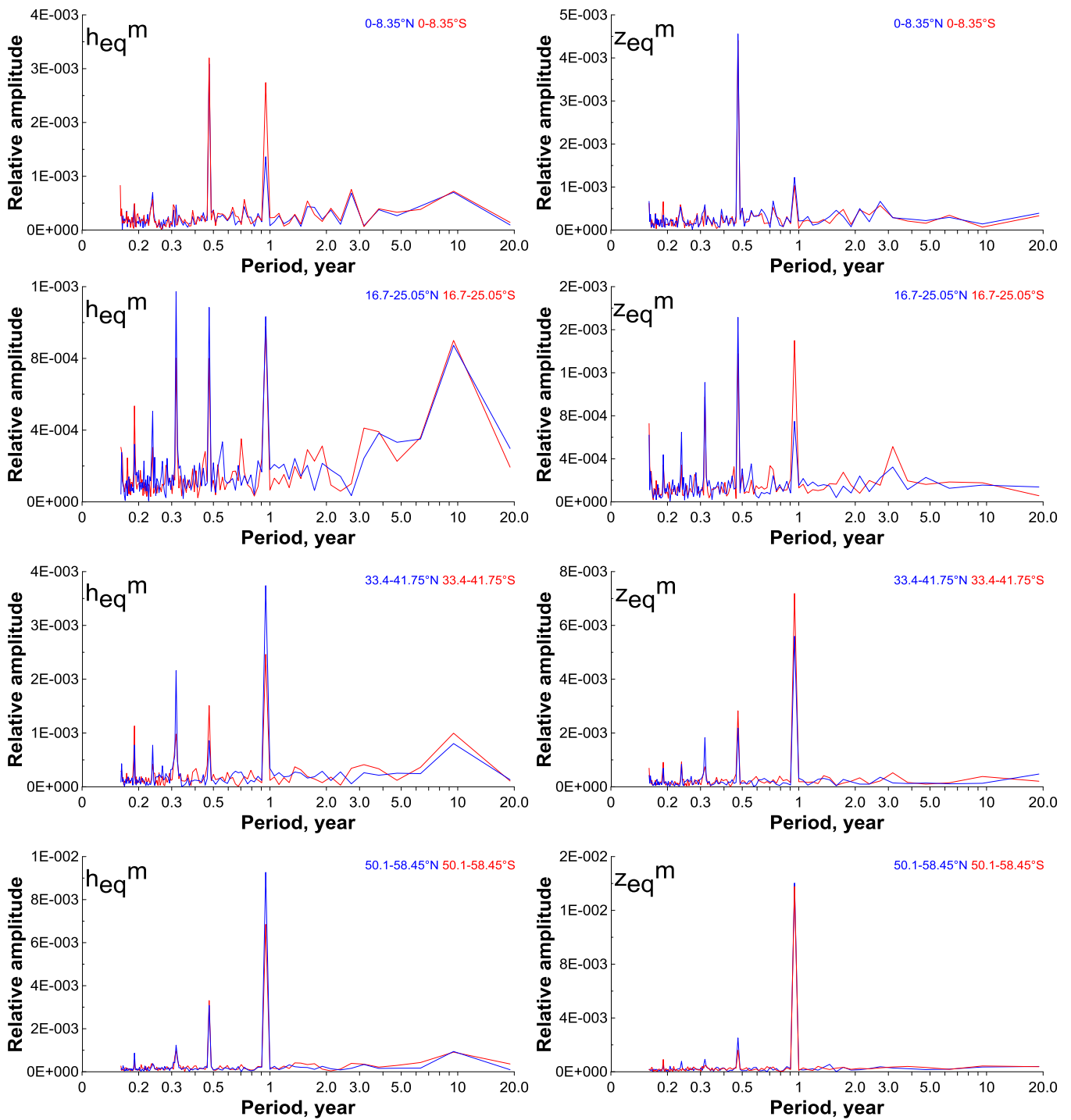
649

650

651

652 Figure 5. Average (for 2002-2021) annual cycle of monthly mean pressure altitude h_{eq}^m and geometrical
 653 altitude z_{eq}^m at four specific latitudes.

654



655

656

657

658

659

660

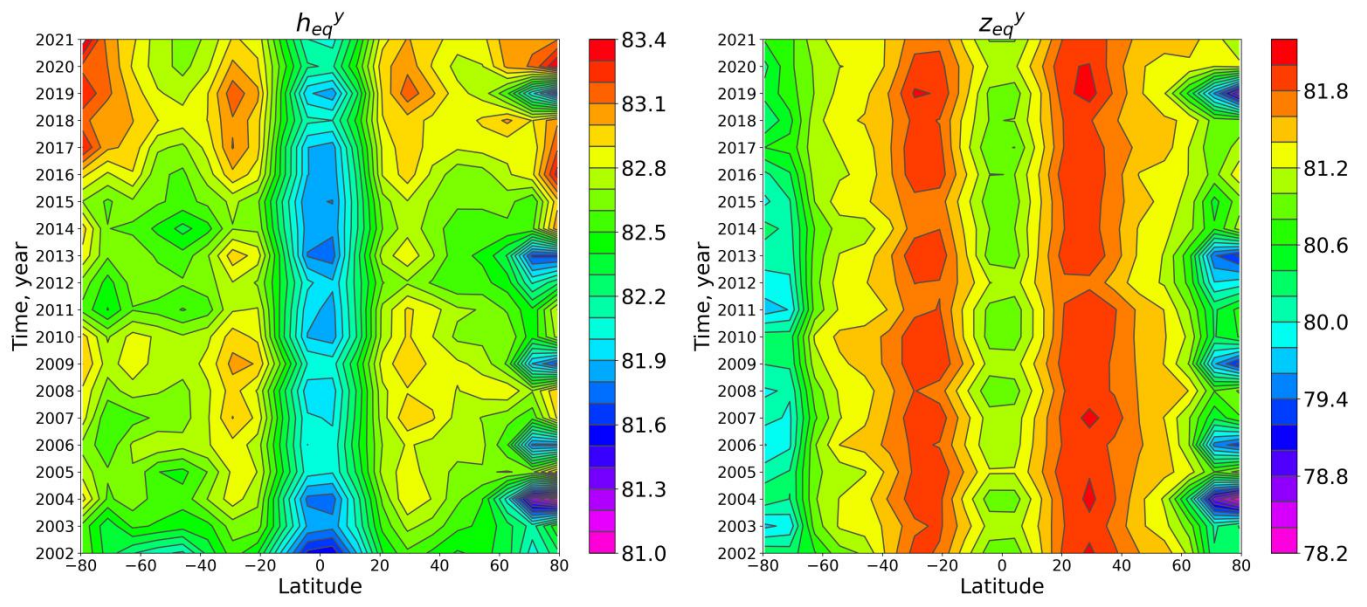
661

662

663

Figure 6. Fourier spectra of monthly mean pressure altitude h_{eq}^m and geometrical altitude z_{eq}^m at four specific latitudes. In each spectrum, the amplitudes of harmonics were normalized to the corresponding zero harmonic.

664

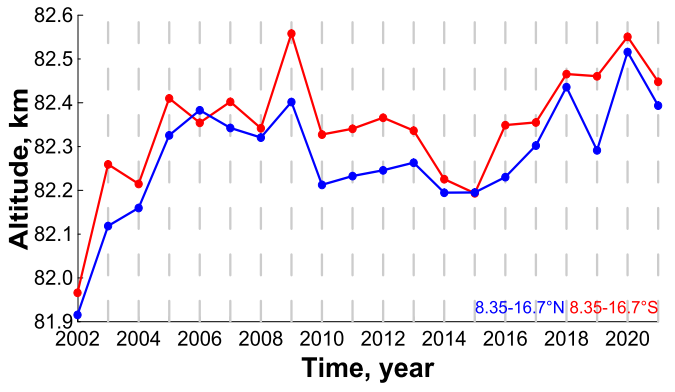
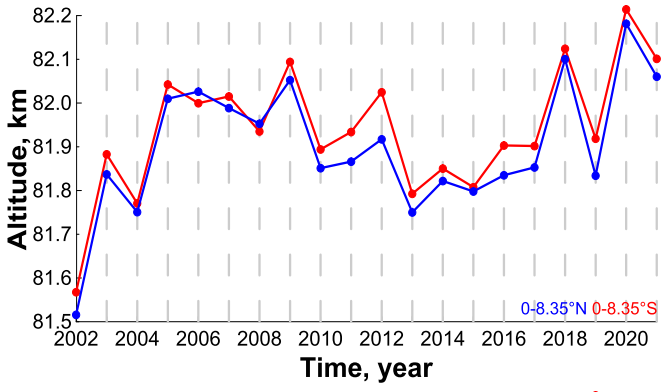


665

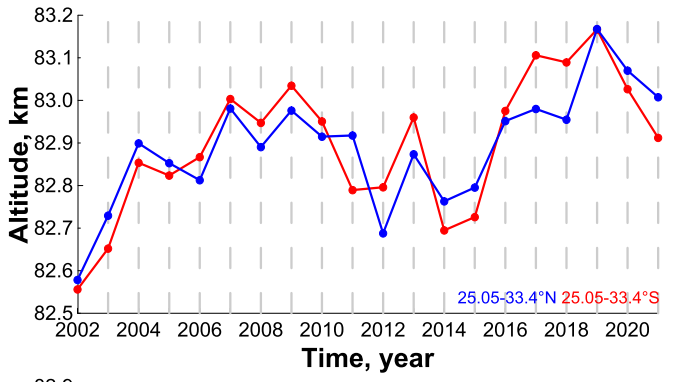
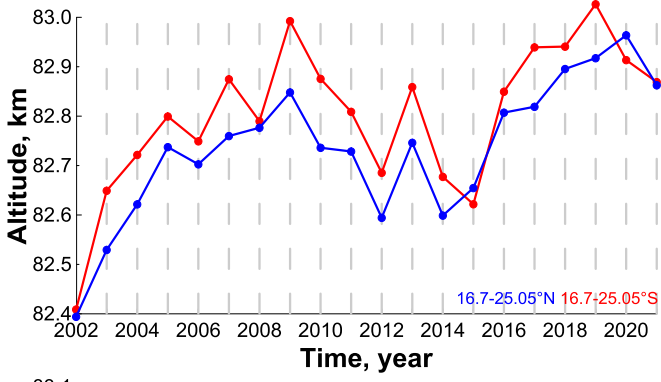
666 Figure 7. Latitude-time evolution of annually mean pressure altitude h_{eq}^y (left) and geometrical altitude
667 z_{eq}^y (right).

668

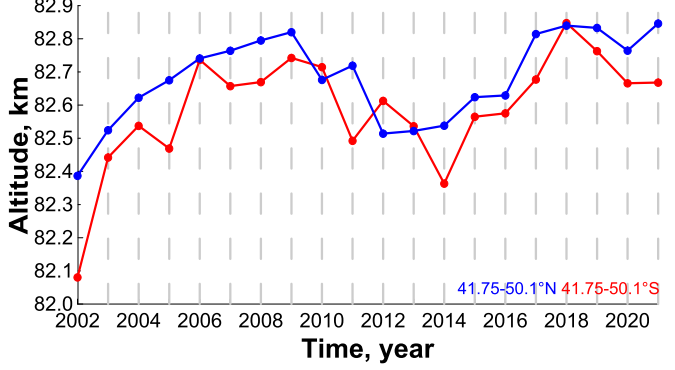
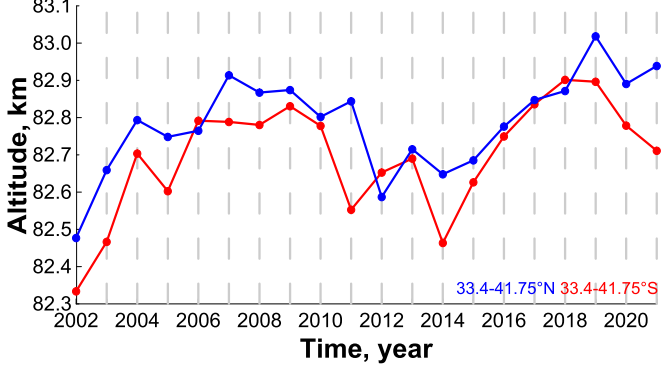
669



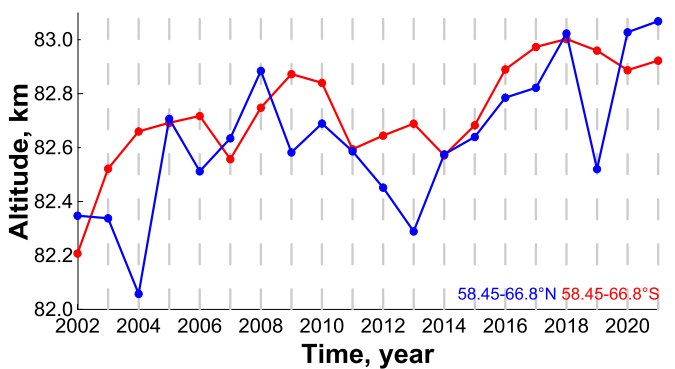
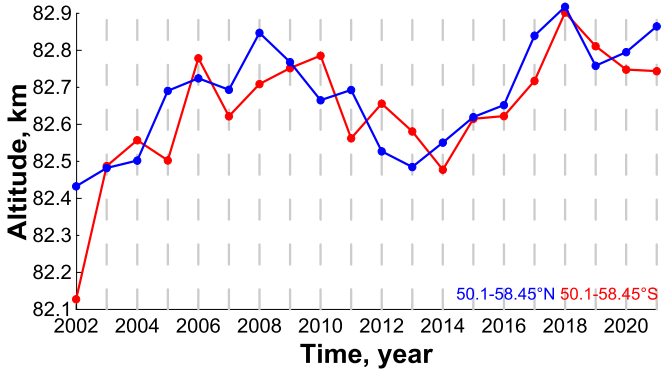
670



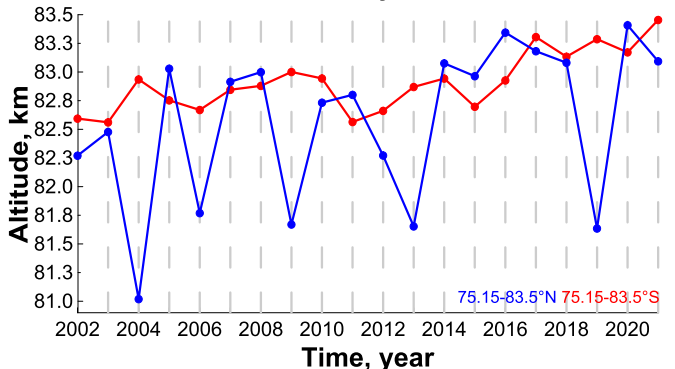
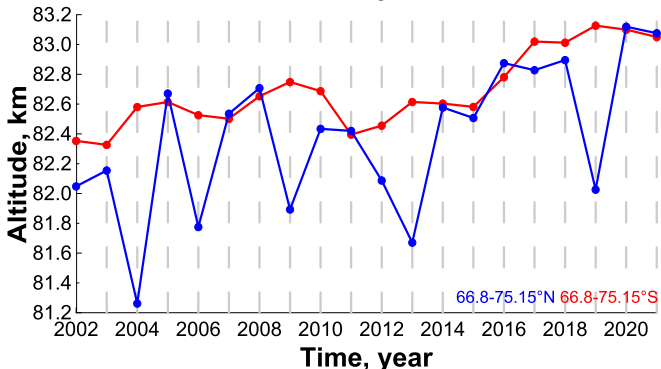
671



672

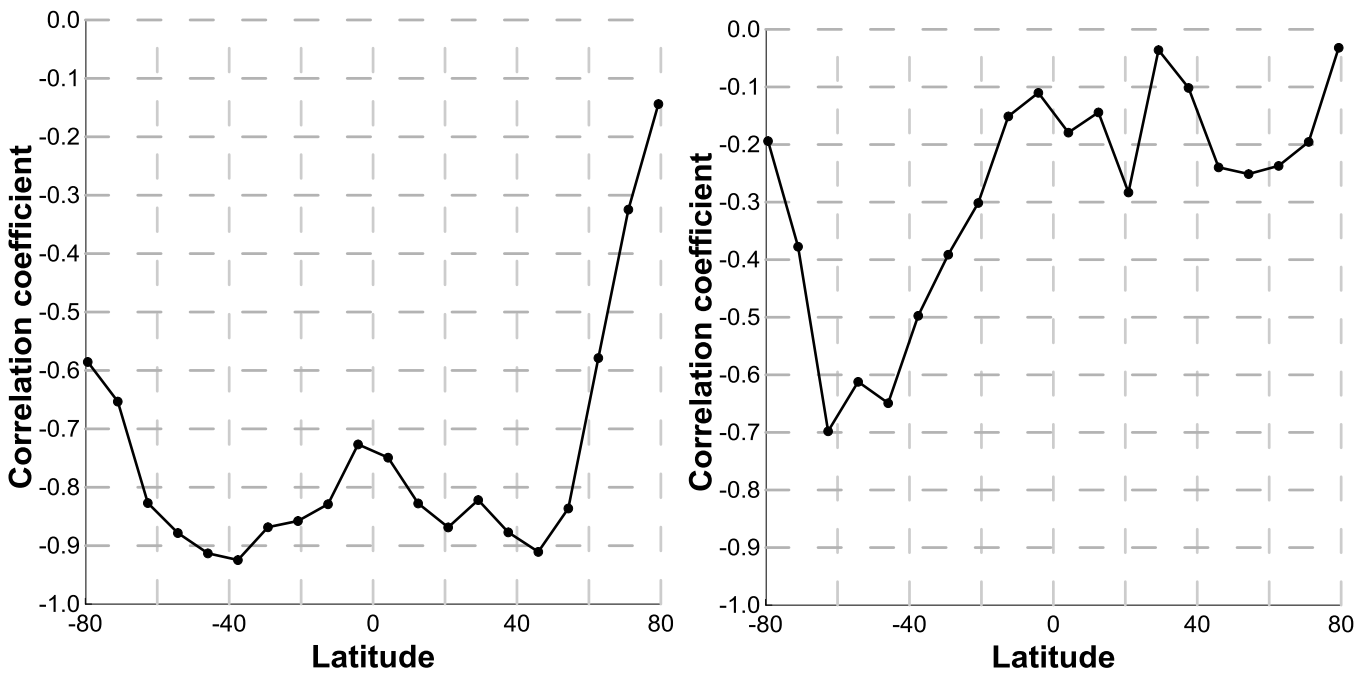


673



674

Figure 8. Time evolution of annually mean pressure altitude h_{eq}^y at different latitudes.



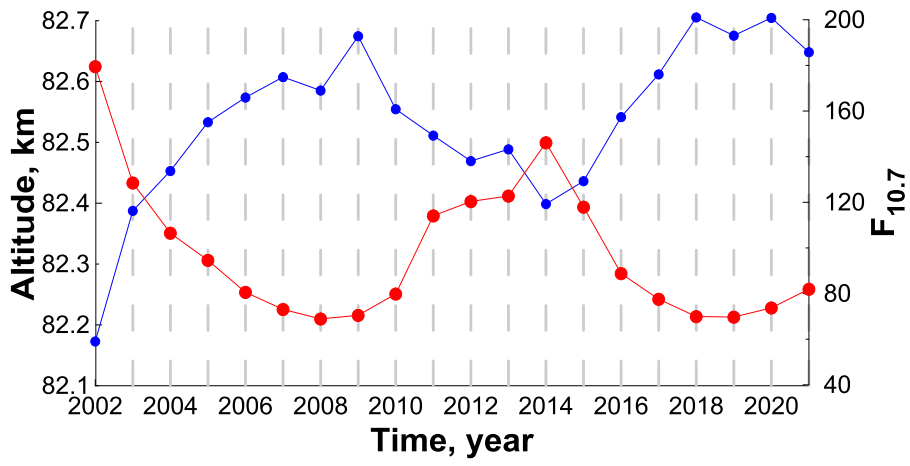
675

676 Figure 9. Correlation coefficient of $F_{10.7}$ index with pressure altitude h_{eq}^y (left) and geometrical altitude

677 z_{eq}^y (right) as a function of latitude.

678

679



680

681

682 Figure 10. Red curve: $F_{10.7}$ index (solar radio flux at 10.7 cm). Blue curve: latitude-averaged pressure
683 altitude h_{eq}^y in the range between $\sim 55^\circ\text{S}$ and $\sim 55^\circ\text{N}$.

684

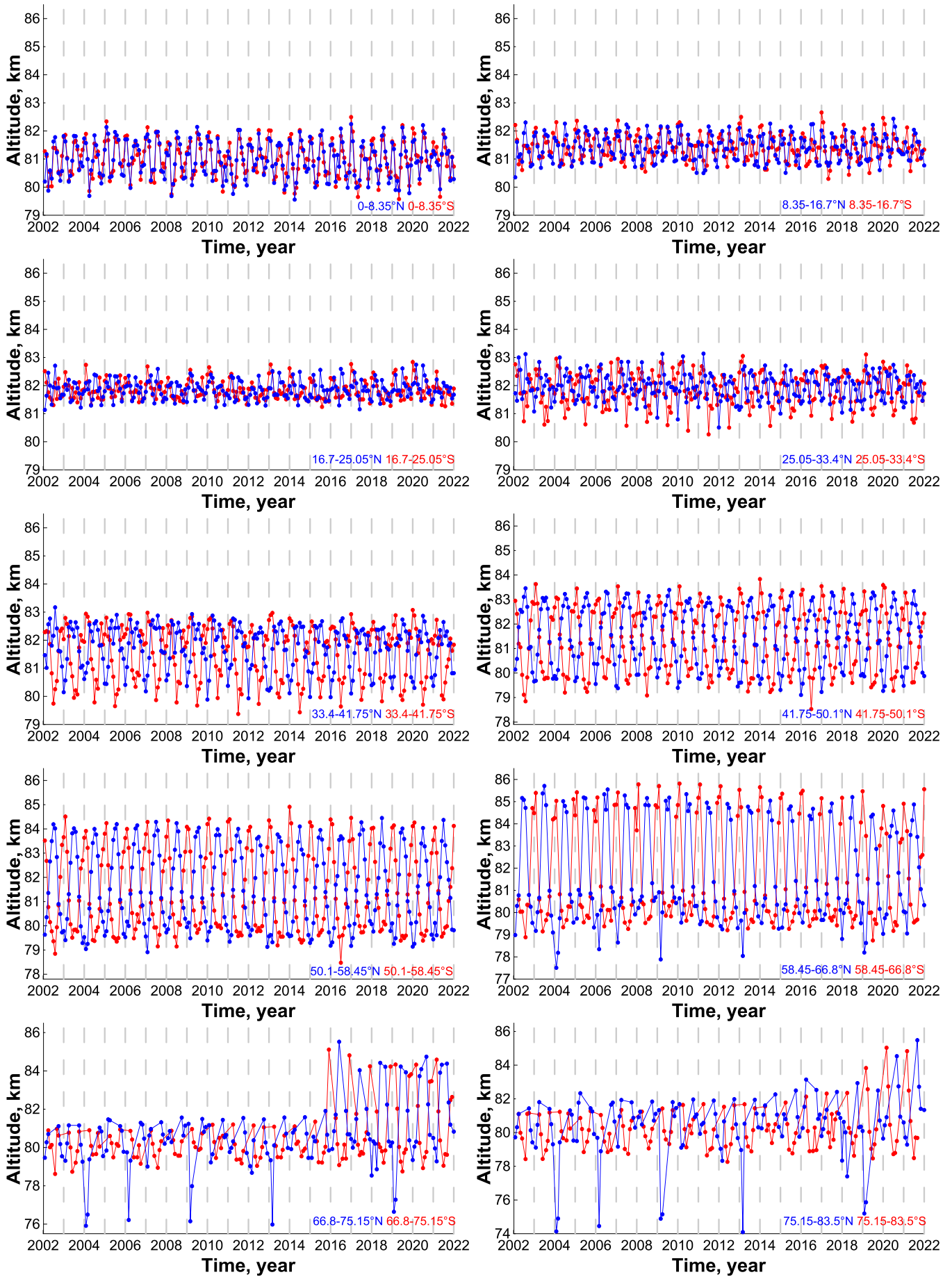
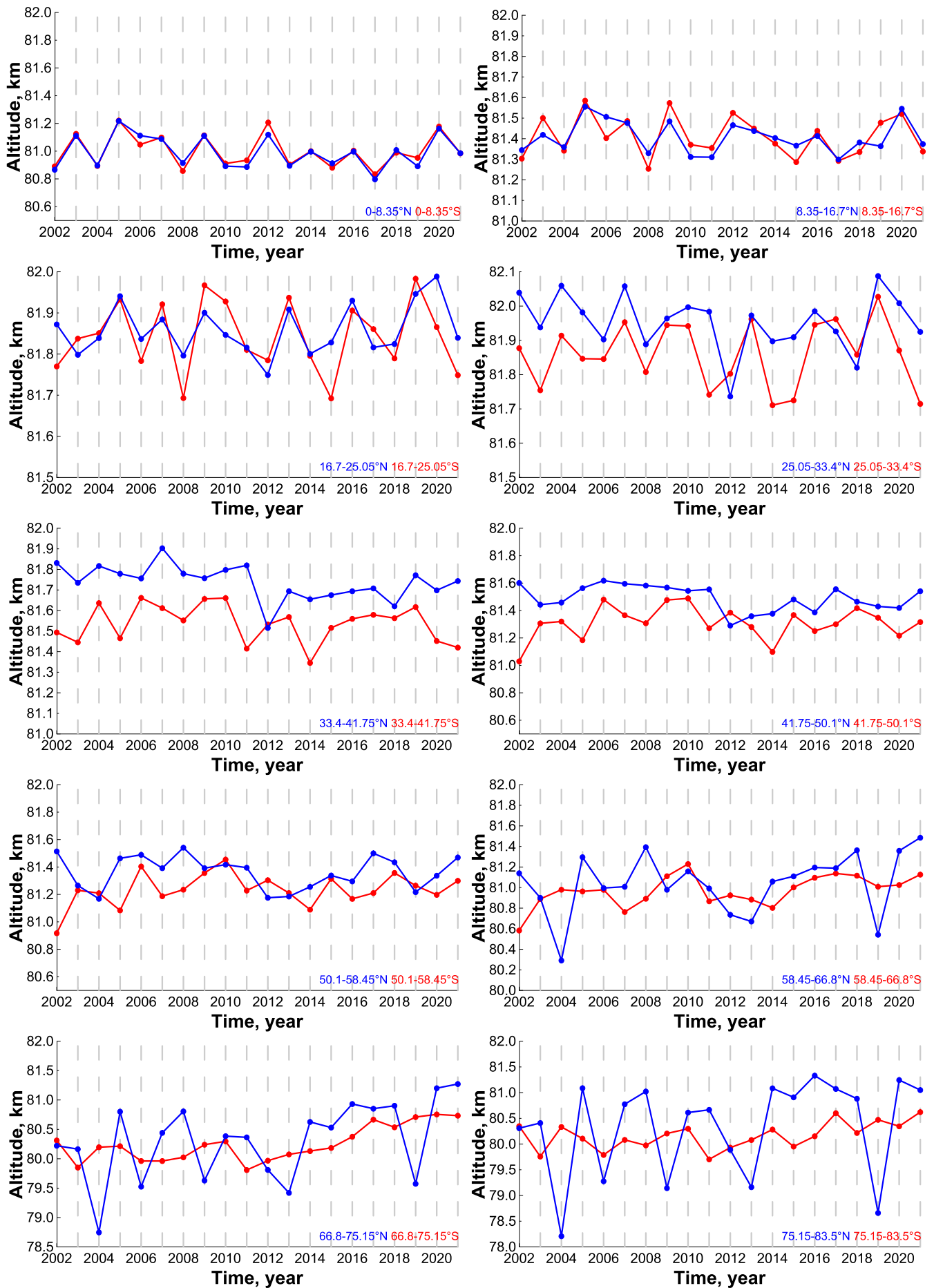


Figure 11. Time evolution of monthly mean geometrical altitude z_{eq}^m at different latitudes.



692

693

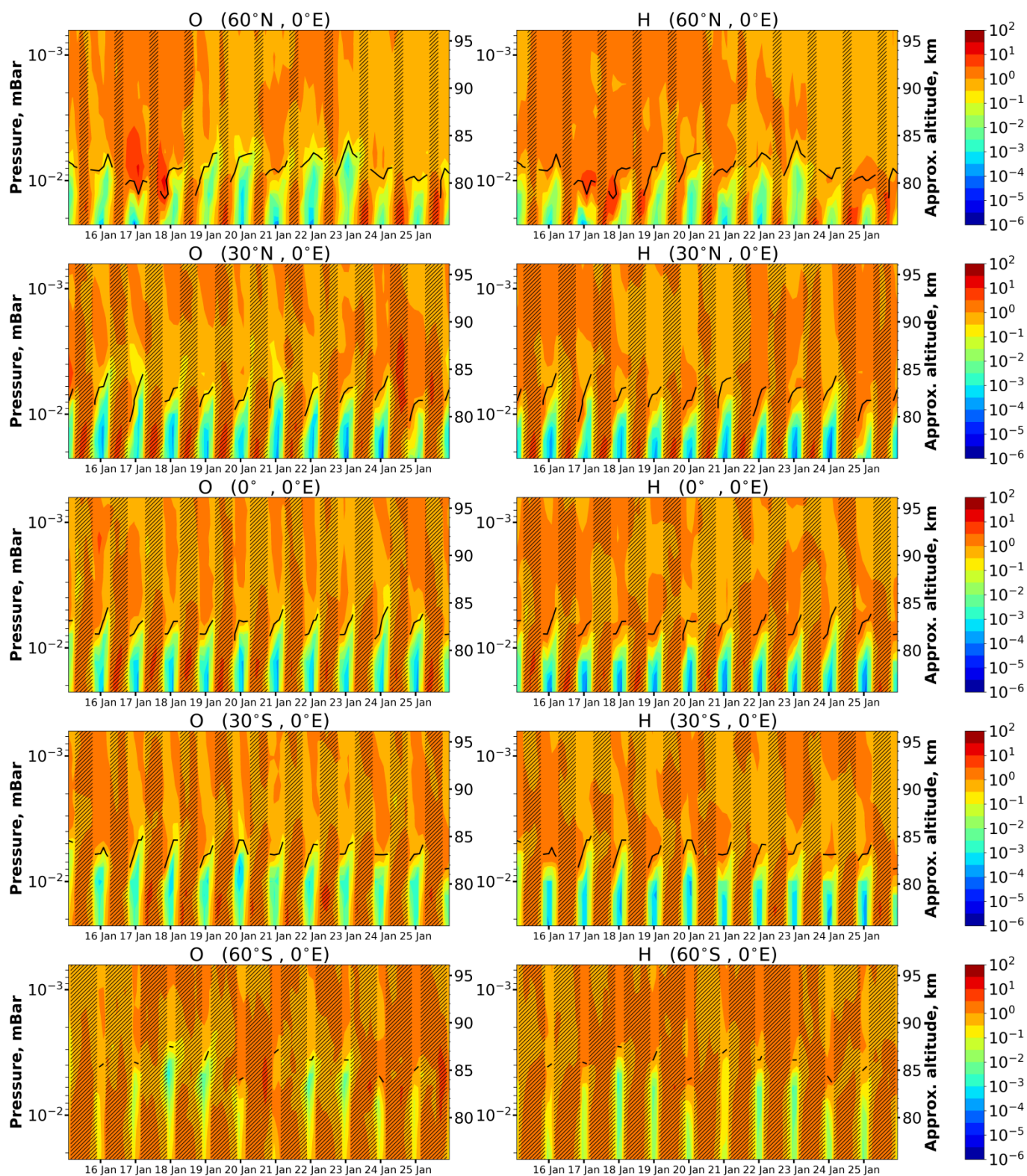
694

695

696

697

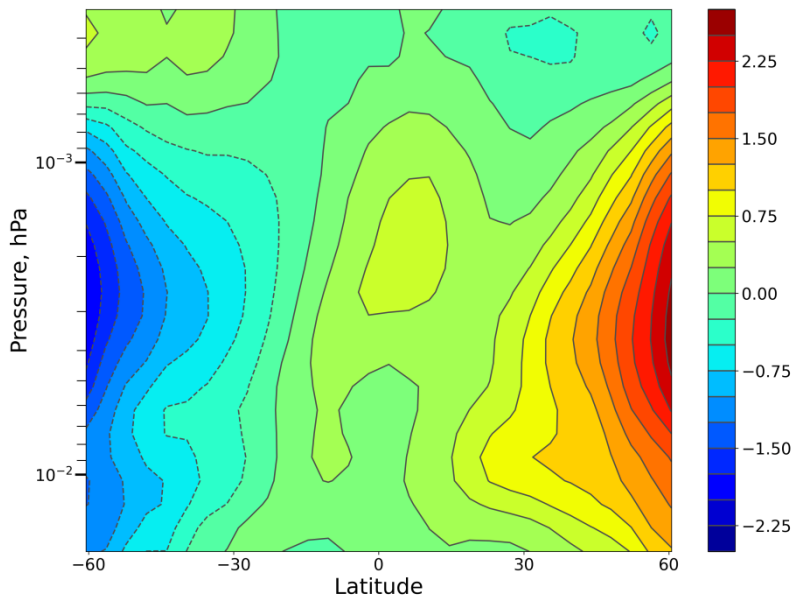
Figure 12. Time evolution of annually mean geometrical altitude z_{eq}^y at different latitudes.



698

699 Figure 13. O and H time-height variations above different points in January 2017 calculated by SD-WACCM-X
 700 model. Concentrations are normalized by mean daily values, correspondingly. Dark bars mark daytime, light bars
 701 mark nighttime. Black lines point the NOCE boundary altitude according to criterion (5) ($Cr = 0.1$).

702



703

704 Figure 14. Logarithm of the ratio of $(O/H)_w$ and $(O/H)_s$ distributions obtained with the use of daytime
 705 seasonally mean distributions of O and H averaged in 2003-2015. $(O/H)_w$ was determined from the
 706 SABER data measured in December, January, and February. $(O/H)_s$ was determined from the SABER
 707 data measured in June, July, and August.